

Contents

1	Introduction and theory overview	1
1.1	Introduction	1
1.2	Theory overview	1
1.2.1	Model of excited leptons	2
1.2.2	Decay of excited leptons	4
1.2.3	Production of excited leptons	8
2	CMS detector and LHC	11
2.1	Large Hadron Collider	11
2.2	CMS detector	12
2.2.1	Coordinate in CMS	13
2.2.2	Superconduction solenoid	14
2.2.3	Tracking system	15
2.2.4	Electromagnetic calorimeter	16
2.2.5	Hadron calorimeter	18
2.2.6	Muon chamber	18
2.3	Trigger system	21
3	Analysis Procedures	23
3.1	Data and Monte-Carlo samples	23
3.1.1	Data samples	23
3.1.2	Monte Carlo samples	24
3.2	Trigger	26

3.3	Object reconstruction and identification	27
3.3.1	Electron reconstruction	27
3.3.2	Electron identification	29
3.3.3	Muon reconstruction	31
3.3.4	Muon identification	32
3.3.5	Pileup Reweighting	38
3.4	Event selection	39
3.4.1	Analysis strategy	39
3.4.2	Background estimation	44
3.5	Systematic uncertainties	54
4	Results and conclusion	57
4.1	Cross section limit computation	57
4.2	Optimization of the final selection	58
4.3	Limit computation	61
4.3.1	Limits for excited muons μ^*	61
4.3.2	Limits for excited leptons e^*	61
4.4	Conclusion	65

List of Figures

1-1	Diagrams showing excited leptons interaction vertices. (a) Gauge interaction between two excited leptons. (b) Gauge interaction between excited lepton and standard model lepton. (c) Four-fermion contact interaction.	5
1-2	Feynman Diagrams for the investigated l^* channels. (a) Excited muon. (b) Excited electron.	6
1-3	Branching ratios of charged excited leptons as function of f/f' with $\Lambda = 10\text{TeV}$ and $M_{l*} = 2\text{TeV}$	7
1-4	Branching ratios of charged excited leptons as function of M_{l*} with $\Lambda = 10 \text{ TeV}$ and $f = f' = 1$	8
1-5	Branching ratios of charged excited leptons as function of M_{l*} with $\Lambda = 10 \text{ TeV}$ and $f = -f' = -1$	9
1-6	Cross section of charged excited leptons production as function of M_{l*} with $\Lambda = 10 \text{ TeV}$	10
2-1	The Large Hadron Collider.	12
2-2	The Compact Muon Solenoid.	14
2-3	The tracker layout of CMS.	16
2-4	Pixel detector inside tracker.	17
2-5	The layout of muon chambers in CMS.	19
2-6	The trigger system in CMS.	22

3-1	The comparison of different trigger efficiencies as a function of excited lepton mass for both $2e2\mu$ channels. Top: $ee^* \rightarrow 2e2\mu$ channel. Bottom: $\mu\mu^* \rightarrow 2\mu2e$ channel.	28
3-2	Efficiency of the isolation cut as a function of ΔR for electrons (top) and muons (bottom) for the non-Z pair with standard ID and the Z pair with boosted Z ID.	34
3-3	Number of Vertices distribution after PileUp reweighting for $\mu\mu^* \rightarrow \mu\mu Z \rightarrow 2\mu2e$ (left), and $ee^* \rightarrow eeZ \rightarrow 2e2\mu$ (right).	38
3-4	Total signal acceptance times efficiency ($Ax\epsilon$) for the all selection criteria before final selection for the various signal samples.	43
3-5	Geometrical acceptance for all channels as given in the legend, with 4 muons and 2e2mu in the final state.	43
3-6	Lepton p_T before invariant mass cuts. Left: $\mu\mu^* \rightarrow 2\mu2e$ channel, Right: $ee^* \rightarrow 2e2\mu$ channel	45
3-7	Lepton η before invariant mass cuts. Left: $\mu\mu^* \rightarrow 2\mu2e$ channel, Right: $ee^* \rightarrow 2e2\mu$ channel	45
3-8	Lepton ϕ before invariant mass cuts. Left: $\mu\mu^* \rightarrow 2\mu2e$ channel, Right: $ee^* \rightarrow 2e2\mu$ channel	46
3-9	Invariant mass distribution of the selected Z before invariant mass cuts. Left: $\mu\mu^* \rightarrow 2\mu2e$ channel, Right: $ee^* \rightarrow 2e2\mu$ channel	46
3-10	Invariant mass distribution of the vetoed Z before invariant mass cuts. Left: $\mu\mu^* \rightarrow 2\mu2e$ channel, Right: $ee^* \rightarrow 2e2\mu$ channel	47
3-11	Four lepton invariant mass M_{4l} before invariant mass cuts. Left: $\mu\mu^* \rightarrow 2\mu2e$ channel, Right: $ee^* \rightarrow 2e2\mu$ channel	47
3-12	ΔR of the two muons from the Z decay before invariant mass cuts. Left: $\mu\mu^* \rightarrow 2\mu2e$ channel, Right: $ee^* \rightarrow 2e2\mu$ channel	48
3-13	Four lepton invariant mass distribution in $H \rightarrow ZZ \rightarrow 2e2\mu$. The excess can also be observed around peak region.	50
3-14	Minimum invariant mass distribution M_{min}^{3l} after invariant mass cuts. Left: $\mu\mu^* \rightarrow 2\mu2e$ channel, Right: $ee^* \rightarrow 2e2\mu$ channel	52

3-15 Maximum invariant mass distribution M_{max}^{3l} after invariant mass cuts. Left: $\mu\mu^* \rightarrow 2\mu 2e$ channel, Right: $ee^* \rightarrow 2e 2\mu$ channel	52
4-1 2-dimensional minimum-maximum invariant mass distribution after invariant mass cuts for different l^* masses. Left: $\mu\mu^* \rightarrow 2\mu 2e$ channel. Right: $ee^* \rightarrow 2e 2\mu$ channel.	58
4-2 Acceptance \times Efficiency for different cut stages: Lepton selection, Z veto and final selection.	59
4-3 2-dimensional minimum-maximum invariant mass distribution after invariant mass cuts. Left: $\mu\mu^* \rightarrow 2\mu 2e$ channel. Right: $ee^* \rightarrow 2e 2\mu$ channel.	62
4-4 Cross section and Λ limit for $\mu\mu^* \rightarrow 4\mu$	62
4-5 Cross section and Λ limit for $\mu\mu^* \rightarrow 2\mu 2e$	63
4-6 Cross section and Λ limit for $ee^* \rightarrow 4e$	63
4-7 Cross section and Λ limit for $ee^* \rightarrow 2e 2\mu$	64
4-8 Combined cross section and Λ limit for $\mu\mu^* \rightarrow 4l$	64
4-9 Combined cross section and Λ limit for $ee^* \rightarrow 4l$	66

List of Tables

1.1	Quantum numbers of excited leptons.	3
2.1	Parameters of the CMS superconducting solenoid.	15
3.1	Summary of the data samples used in this analysis	24
3.2	Summary of Monte Carlo signal samples, cross sections (LO), and k-factors used for $ll^* \rightarrow llZ \rightarrow 2l2l'$ ($l = e, \mu$ and $l' = e, \mu, \tau$) with $\Lambda = 10$ TeV and $f = f' = 1$. (*) The k-factor for 2600 GeV was calculated by extrapolation [1].	26
3.3	Summary of the used Monte Carlo background samples with the corresponding cross section in NLO.	35
3.4	HEEP electron ID	36
3.5	Scale factors for HEEP electron selection from HEEP group	36
3.6	High pT muon ID	36
3.7	Scale factors for high- p_T muon ID from MUO-POG	37
3.8	Scale factors for $\text{TkRelIso} < 0.1$ from MUO-POG	37
3.9	Scale factors used for the modified muon ID and isolation, taken from $X \rightarrow ZZ \rightarrow qql\bar{l}$ Analysis Note.	37
3.10	Cut Flow Table for $\mu\mu^* \rightarrow \mu\mu Z \rightarrow 2\mu 2e$. The Acceptance step includes two electrons and two muons with $p_T > 25$ GeV in the geometrical acceptance, the ratio is calculated with respect to the full number of events (also those without two electrons and two muons).	41

3.11 Cut Flow Table for $ee^* \rightarrow eeZ \rightarrow 2e2\mu$. The Acceptance step includes two electrons and two muons with $p_T > 25$ GeV in the geometrical acceptance, the ratio is calculated with respect to the full number of events (also those without two electrons and two muons).	42
3.12 Event yields for $\mu\mu^* \rightarrow 4\mu$ and $\mu\mu^* \rightarrow 2\mu2e$ without invariant mass cut. If the column includes 0.00 ± 0.00 events, the calculated number is to small for a prediction.	48
3.13 Events yields for $ee^* \rightarrow 4e$ and $ee^* \rightarrow 2e2\mu$ without invariant mass cut. If the column includes 0.00 ± 0.00 events, the calculated number is to small for a prediction.	49
3.14 Events yields for $\mu\mu^* \rightarrow 4\mu$ and $\mu\mu^* \rightarrow 2\mu2e$ after invariant mass cuts. If the column includes 0.00 ± 0.00 events, the calculated number is to small for a prediction.	51
3.15 Events yields for $ee^* \rightarrow 4e$ and $ee^* \rightarrow 2e2\mu$ after invariant mass cuts. If the column includes 0.00 ± 0.00 events, the calculated number is to small for a prediction.	53
3.16 Summary of systematic uncertainties on signal and background yields for the $\mu\mu^* \rightarrow 2\mu2e$ channel. Here, the two electrons come from the boosted Z and the Z Veto is applied to the muon pair. The uncertainties are the combined ones for all leptons, the considered single lepton uncertainties are summarized in the text.	56
3.17 Summary of systematic uncertainties on signal and background yields for the $ee^* \rightarrow 2e2\mu$ channel. Here, the two muons come from the boosted Z and the Z Veto is applied to the electron pair. The uncertainties are the combined ones for all leptons, the considered single lepton uncertainties are summarized in the text.	56
4.1 Cut ranges for the L shape cuts, corresponding event yields and signal efficiencies $\mu\mu^* \rightarrow 2\mu2e$	59

4.2 Cut ranges for the L shape cuts, corresponding event yields and signal efficiencies $ee^* \rightarrow 2e2\mu$.	60
---	----

Chapter 1

Introduction and theory overview

1.1 Introduction

This thesis presents the result and process of the search for signal of heavy resonances decaying into a Z boson and a Higgs boson (h) final state at center-of-mass energy of 8 TeV, using 19.7 fb^{-1} p-p collision data. In turn, the Z boson is identified through its leptonic decays (leptons often refer to e and μ only in experiments, $l = e, \mu$). The Higgs boson h is expected to hadronically decay primarily into a pair of b-quarks. The investigated final states consists of two b-quarks and two charged leptons.

1.2 Theory overview

The standard model (SM) is a great theory that has successfully explained the interaction between particles and agree with the result from experiments pretty well for past 40 years. However, there are still serveral fundamental questions not explained in SM. One of them is mass hierarchy of quarks and leptons.

A possible solution is to introduce the compositness model [2–4]. In compositness model, quarks and leptons are claimed to be the bound states of some sub-particles. These sub-particles, called preons, are proposed to be bounded by an unknown interaction. The appearance of preons' idea is not surprised. In the past, various atoms are considered to be the basic unit of nature. After people break into the atoms,

they are found to be composed of electrons, protons, and neutrons. Today, protons and neutrons are again known to be compositeness. It's very intuitive to guess that the SM particles are again composed of some more fundamental structure. If the sub-structure of leptons or quarks really exists, the discovery of the excited state can provide a direct proof for compositeness model.

1.2.1 Model of excited leptons

Unlike the search of Higgs boson or other theory such as supersymmetry, compositeness model is not predicted by SM and does not build up a beautiful and giant model. Furthermore, it also unlike the dark matter, which is suggested to be existed by cosmos observation. Despite there has yet a complete model of preons that can satisfies a number of physicists, the search of excited leptons has been performed at LEP, HERA, Tevatron and the LHC before [5–12]. The behavior of the excited leptons in this thesis is simulated by PYTHIA 8 [13], and it uses the phenomenology described in [3].

The weak isodoublets of both left- and right-handed excited lepton of first generation are assigned as follows.

$$l_L^* = e_R \begin{pmatrix} \nu_e^* \\ e^* \end{pmatrix}_L, \quad l_R^* = \begin{pmatrix} \nu_e^* \\ e^* \end{pmatrix}_R$$

It is expected that the excited leptons acquire the mass before $SU(2) \times U(1)$ symmetry breaking. The quantum numbers of excited leptons are fixed to the numbers list in Tab. 1.1. Both the spin and weak isospin is set to 1/2, and hypercharge Y is set to -1.

The coupling of excited leptons is assumed to have a similar form as their SM ground state. Following Lagrangian shows the interaction between two excited leptons mediate by gauge boson.

$$\mathcal{L}_{l^* l^* V} = \bar{l}^* \gamma^\mu \left(g \frac{\tau}{2} W_\mu + g' \frac{Y}{2} B_\mu \right) l^* \quad (1.1)$$

	Y	T	T_3	Q
ν_{eL}^*	-1	$\frac{1}{2}$	$\frac{1}{2}$	0
e_L^*	-1	$\frac{1}{2}$	$-\frac{1}{2}$	-1
ν_{eR}^*	-1	$\frac{1}{2}$	$\frac{1}{2}$	0
e_R^*	-1	$\frac{1}{2}$	$-\frac{1}{2}$	-1

Table 1.1: Quantum numbers of excited leptons.

Due to the composite nature of the model, each interaction above should be corrected by a set of form factors. However, for a large value of the compositeness scale Λ , the effect of form factors are negligible.

Gauge bosons can also mediate the transitions between right-handed excited leptons and left-handed SM leptons. This interaction leaves a signature to discover excited lepton by searching for resonance of SM leptons. The Lagrangian of excited leptons transition is written as below

$$\mathcal{L}_{l^*lV} = \frac{1}{2\Lambda} \bar{l}_R^* \sigma^{\mu\nu} \left(g f \frac{\tau}{2} W_{\mu\nu} + g' f' \frac{Y}{2} B_{\mu\nu} \right) l_L + h.c. \quad (1.2)$$

In this Lagrangian, there are two constant parameters f and f' , which determines the coupling strength of different gauge fields. These two parameters are both expected to be of order 1. In this study, the final limits of excited electrons and muons are presented under the condition assuming $f = f' = 1$ and $f = -f' = -1$.

The excited leptons may couple to SM lepton via four-fermion contact interaction source by an unknown interaction beyond SM. For energies below compositeness scale Λ , they can be described by the following Lagrangian.

$$\mathcal{L}_{CI} = \frac{g^{*2}}{2\Lambda^2} j^\mu j_\mu \quad (1.3)$$

The g^{*2} here is chosen to have value 4π . j^μ is the lepton current with the form

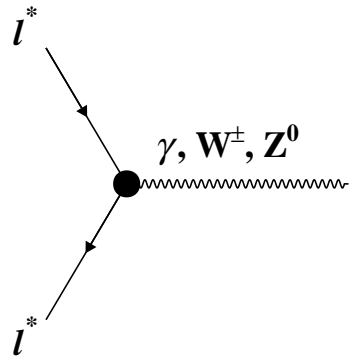
$$j_\mu = \eta_L \bar{f}_L \gamma_\mu f_L + \eta'_L \bar{f}_L^* \gamma_\mu f_L^* + \eta''_L \bar{f}_L^* \gamma_\mu f_L + h.c. + (L \rightarrow R) \quad (1.4)$$

The η factors of left-handed currents are set to be one for simplicity, and the right-handed terms are therefore become zero to reserve chiral symmetry [14]. The f and f^* show in above equation represent fermion and excited fermion respectively. The use of “fermion” instead of “lepton” in the contact interaction Lagrangian is because of the production of excited leptons in LHC require to include the coupling of excited leptons and quarks. Leptons and quarks are assumed to be composed of same set of preons in current model, thus it is possible to have such a four-fermion contact interaction that directly couples quarks to leptons with any combination between excited and SM particles.

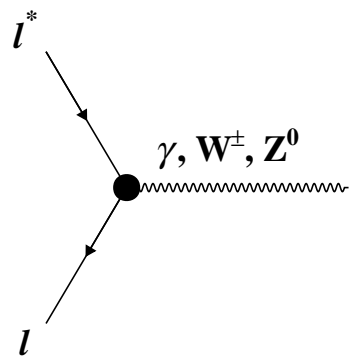
Fig. 1-1 summarize the vertices introduced in above three Lagrangians. The interested process of the search with four-lepton final state in CMS is shown in Fig. 1-2. Excited leptons in this search are produced by contact interaction with a SM partner with same flavor, and transit to SM lepton via Z emission. Furthermore, the emitted Z with electron or muon decay is chosen for it provide a clean signature. The choice of Z-mediated channel is due to the relative less background events compares to γ -mediated channel, and is never been tried in LHC before, though the cross section is relative smaller. The reason of the pair production, which produced two excited leptons in one collision, is not considered in this search is that the cross section of the pair production is much smaller than the single production and can hardly raise the event yields. More details about production rate will be introduced in Sec. 1.2.3.

1.2.2 Decay of excited leptons

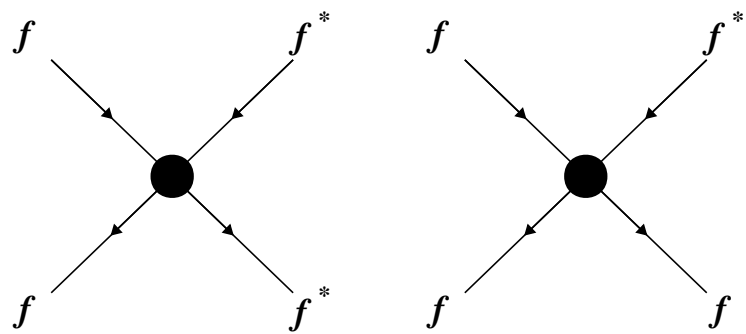
Heavy excited leptons are expected to decay into SM leptons in a sudden they produced. The decay can occur via emitting a gauge bosons or four-fermion contact interaction. For the excited lepton mass greater than the vector bosons mass ($M_{l_*} > M_V$),



(a)



(b)



(c)

Figure 1-1: Diagrams showing excited leptons interaction vertices. (a) Gauge interaction between two excited leptons. (b) Gauge interaction between excited lepton and standard model lepton. (c) Four-fermion contact interaction.

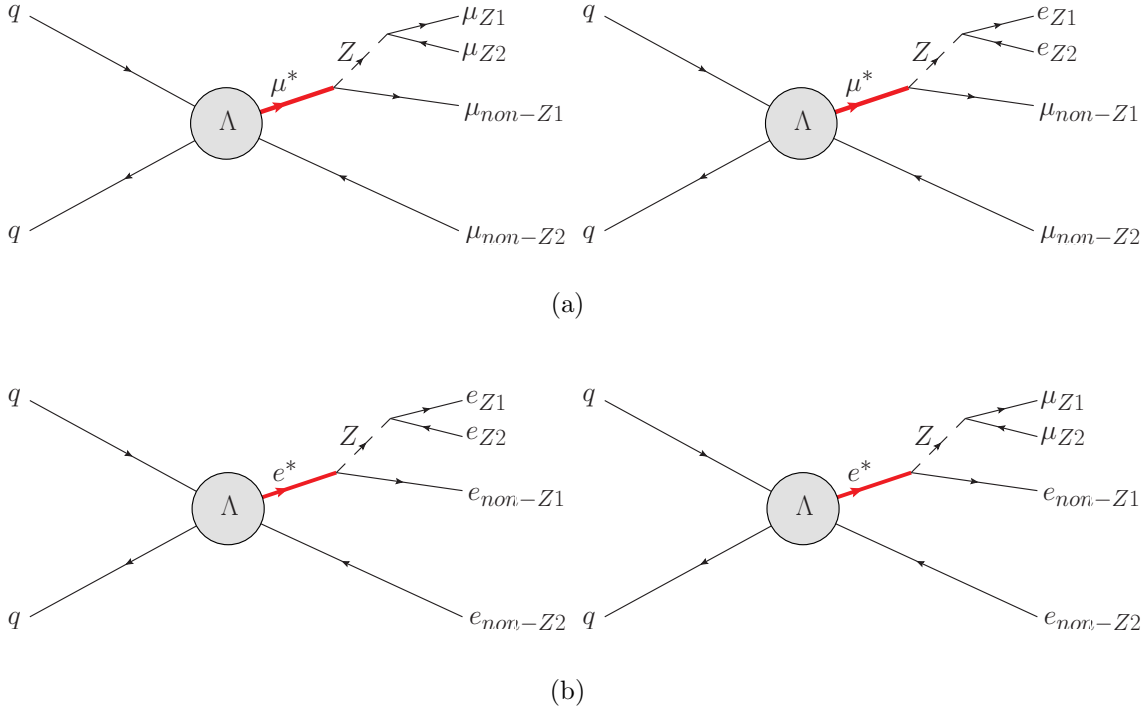


Figure 1-2: Feynman Diagrams for the investigated l^* channels. (a) Excited muon.
(b) Excited electron.

the partial widths of each gauge-mediated channels are shown in following equations.

$$\Gamma(l^* \rightarrow lV) = \frac{1}{8} \frac{g_V^2}{4\pi} f_V^2 \frac{M_{l^*}^3}{\Lambda^2} \left(1 - \frac{M_V^2}{M_{l^*}^2}\right)^2 \left(2 + \frac{M_V^2}{M_{l^*}^2}\right) \quad (1.5)$$

with

$$f_\gamma = fT_3 + f' \frac{Y}{2} \quad (1.6)$$

$$f_Z = fT_3 \cos^2 \theta_W - f' \frac{Y}{2} \sin^2 \theta_W \quad (1.7)$$

$$f_W = \frac{f}{\sqrt{2}} \quad (1.8)$$

Here, g_V denotes the corresponding coupling constants of each vector boson. For contact interaction, the width is obtained by

$$\Gamma(l^* \rightarrow l f \bar{f}) = \frac{M_{l^*}}{96\pi} \left(\frac{M_{l^*}}{\Lambda}\right)^4 N_c S' \quad (1.9)$$

The S' is an additional combinatorical factor that $S' = 2$ when $f = l$, and $S' = 1$ otherwise. The N_c represents the numbers of color. $N_c = 1(3)$ for f represents a lepton(quark).

From above equations, it can be seen that the branching ratio of each possible decay channel depends strongly on the value of coupling strength constants, f and f'), and the ratio of excited lepton mass over the compositeness scale(M_{l*}/Λ). Fig. 1-3 shows the branching ratios of each decay mode of charged excited leptons with different f/f' values. The different assumptions of f and f' will result in different branching ratios among channels, and finally affect the limit setting. All gauge-mediated channels obtain a certain value of f/f' that the process is totally forbidden. For example, in the case of $f = -f' = -1$, the photon-mediated channel gives out a partial width of zero. This gives rises of the higher branching ratios of the Z-mediated channel, and can therefore reach a higher upper limit in this study than the case where $f = f' = 1$ if no discovery claimed.

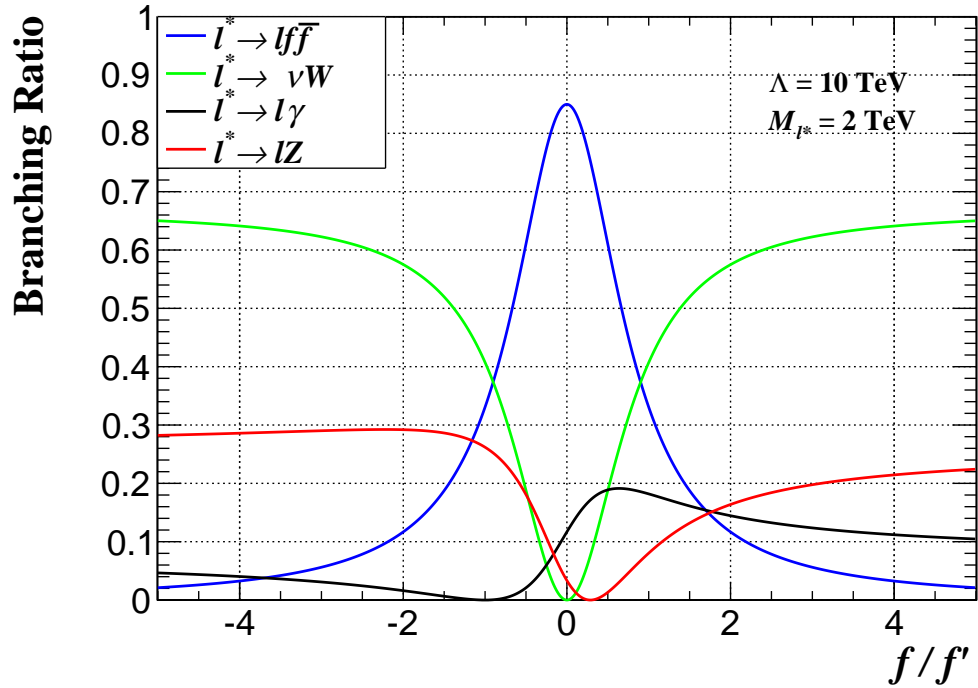


Figure 1-3: Branching ratios of charged excited leptons as function of f/f' with $\Lambda = 10\text{TeV}$ and $M_{l*} = 2\text{TeV}$.

Fig. 1-4 and Fig. 1-5 shows the mass dependence of branching ratios with $f = f'$ and $f = -f'$ respectively for charged excited leptons. The cross-over structure for charged excited leptons with low mass is due to the square damping term in f_V . The decay via contact interaction becomes dominant as the M_{l^*} approaches the Λ , due to the different dependence on M_{l^*}/Λ compare to gauge-mediated channels. For $M_{l^*} = \Lambda$, the branching ratio of contact interaction reaches a value of 0.92, and only 0.08 for the sum of all gauge-mediated channels.

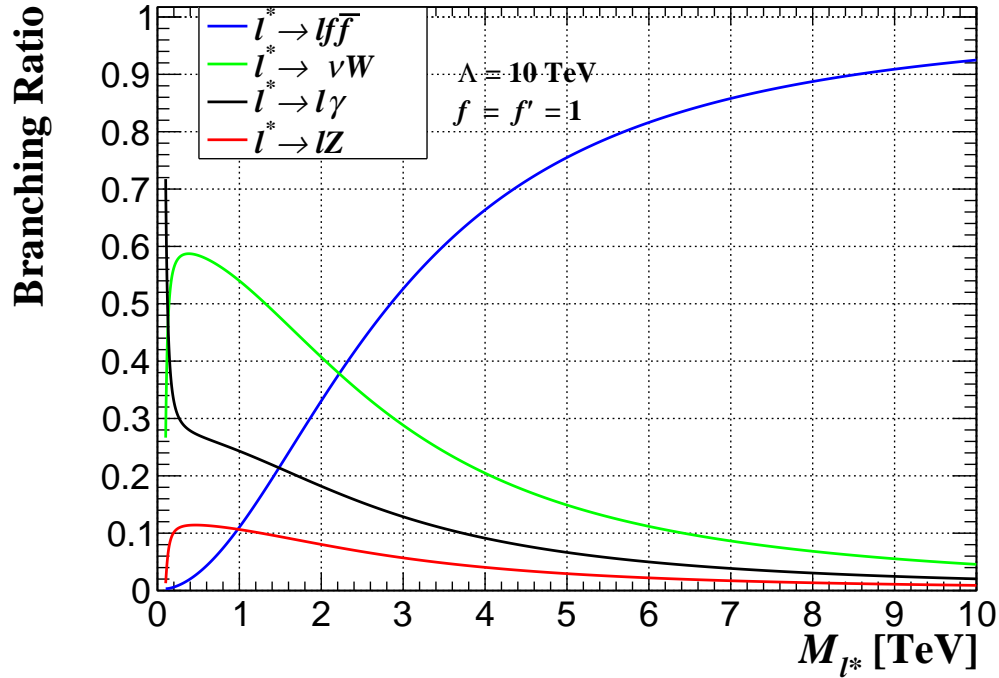


Figure 1-4: Branching ratios of charged excited leptons as function of M_{l^*} with $\Lambda = 10$ TeV and $f = f' = 1$.

1.2.3 Production of excited leptons

Excited leptons can be produced singly or pairily through contact interactions in p-p collisions as shown in Fig. 1.2.1. Base on the Lagrangian of the contact interaction, the cross section of excited lepton production can be obtained by

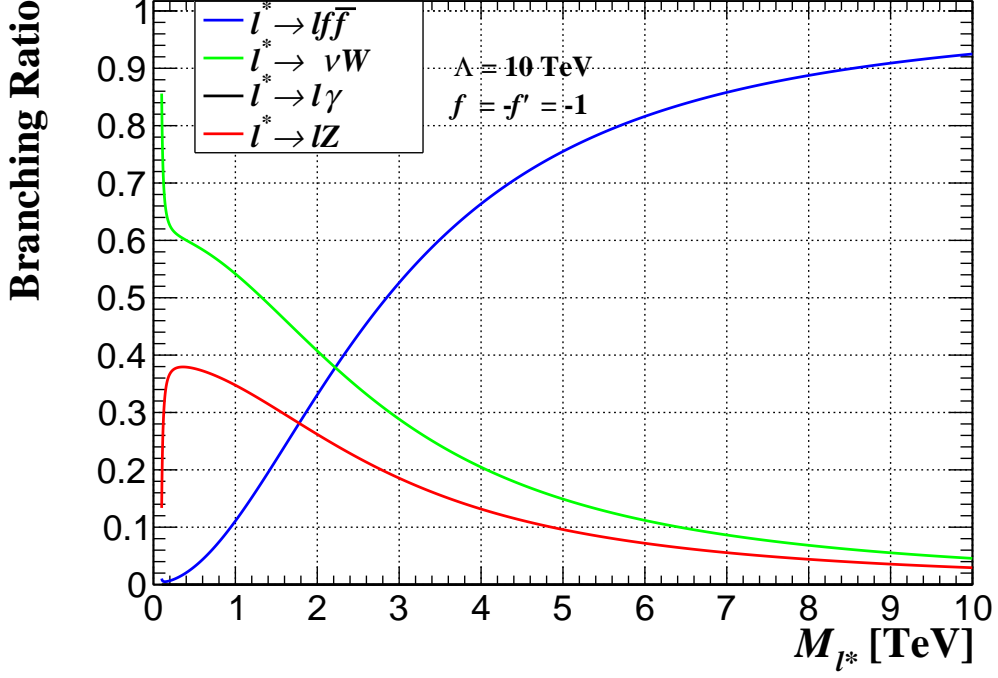


Figure 1-5: Branching ratios of charged excited leptons as function of M_{l^*} with $\Lambda = 10$ TeV and $f = -f' = -1$.

$$\sigma_{single}(q\bar{q} \rightarrow l^*\bar{l}, l\bar{l}^*) = \frac{\pi}{6s} \left(\frac{s}{\Lambda^2} \right)^2 \left(1 + \frac{1}{3} \frac{s - M_{l^*}^2}{s + M_{l^*}^2} \right) \left(1 - \frac{M_{l^*}^2}{s} \right)^2 \left(1 + \frac{M_{l^*}^2}{s} \right) \quad (1.10)$$

and

$$\sigma_{pair}(q\bar{q} \rightarrow l^*\bar{l}^*) = \frac{\pi}{9s} \left(1 - 4 \frac{M_{l^*}^2}{s} \right)^{\frac{1}{2}} \left(\frac{s}{\Lambda^2} \right)^2 \left(1 - \frac{M_{l^*}^2}{s} \right) \quad (1.11)$$

Fig. 1-6 shows the cross section of the excited leptons single and pair production with $\Lambda = 10$ TeV. It can be seen that the cross section of single production is much larger than pair production. Moreover, the pair production will lead to rather complicate final states, and it is not too possible that a pair product events being removed with single production selection. Therefore, the normal strategy of the ex-

cited leptons search aims to search for single production events only.

The cross section describe in this section is just a theoretical prediction of the excited leptons production. The actual used cross section in the experiments need further multiply a proper branching ratio depends on different final states and a leading order(LO) to next-to-leading order(NLO) correction factor. This cross section will be revealed in Sec. 3.1.

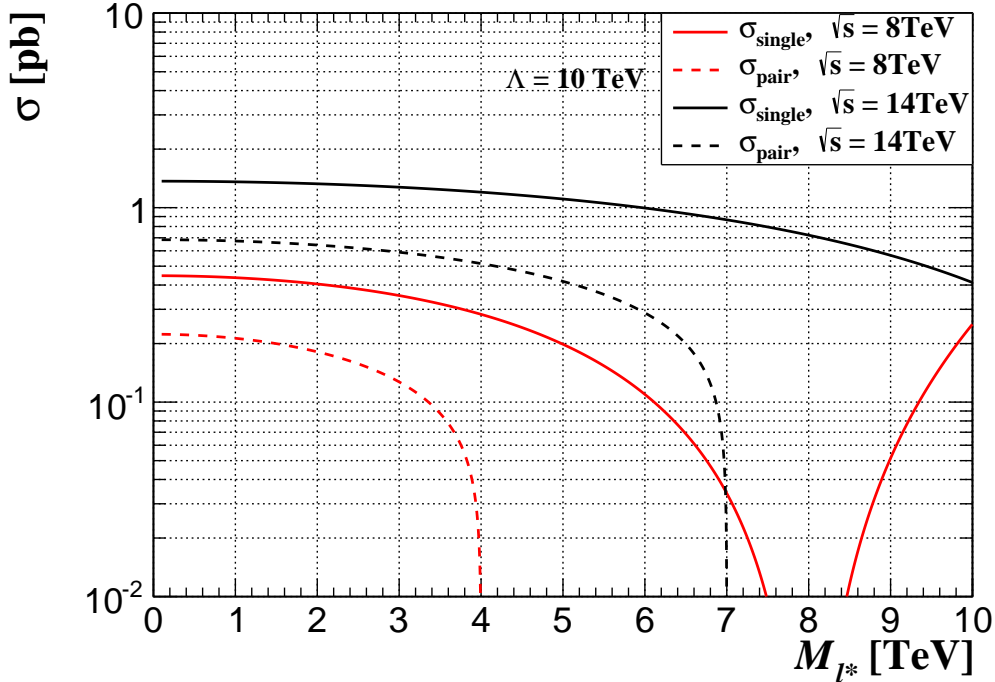


Figure 1-6: Cross section of charged excited leptons production as function of M_{l^*} with $\Lambda = 10$ TeV.

Chapter 2

CMS detector and LHC

TESThis analysis is done by using the data recorded by the Compact Muon Solenoid(CMS) detector at Large Hadron Collider(LHC). CMS is one of the two biggest experiments in LHC, and is involved in the discovery of Higgs boson in July, 2011. In this chapter, the brief overview of LHC and CMS detector will be introduced.

2.1 Large Hadron Collider

The LHC is the biggest particle accelerator that humans ever built on earth. The construction of the LHC started from 1998 and ended in 2008. Fig. 2-1 shows the overview of LHC. The LHC is designed to have 27 km in circumference lies in a ring tunnel hundred meters underground acrossing French-Swiss border. It is a proton-proton collider. The designed top collision energy is 14 TeV and can afford luminosity up to $10^{-34} cm^{-2}s^{-1}$. Few days after its first operation in November 2009, the center-of-mass energy per beam reached 1.18 TeV, breaking the record held by Tevatron in Fermilab becoming the most powerful particle accelerator in world till today.

There are four collision points at LHC, corresponding to four main experiments. They are CMS, ATLAS, ALICE, and LHCb respectively. The ALICE and the LHCb experiments are for specific studies. The ALICE experiment put the sight on heavy ion collisions, learning the matters in high density conditions. The LHCb experiment aims to find the clues of matter and anti-matter's mystery by observing the production and



Figure 2-1: The Large Hadron Collider.

decay of b quarks. Last, the CMS and the ATLAS are the two biggest experiments at LHC, and their detector design are for general purpose. They involved in any kind of search in high energy physics, such as SUSY, dark matter, or other exotica particles, and most importantly, the discovery of Higgs boson in July, 2012.

2.2 CMS detector

The design of CMS has to satisfy the requirements below to make it a discovery machine.

- Good muon identification and momentum resolution over a wide range of momenta in the region $|\eta| < 2.5$, good dimuon mass resolution, and the ability to determine unambiguously the charge of muons at high momentum.

- Good charged particle momentum resolution and reconstruction efficiency in the inner tracker.
- Good electromagnetic energy resolution, good diphoton and dielectron mass resolution, wide geometric coverage ($|\eta| < 2.5$), measurement of the direction of photons and/or correct localization of the primary interaction vertex, π^0 rejection and efficient photon and lepton isolation at high luminosities.
- Good Missing transverse energy and dijet mass resolution.

The construction, installation and commissioning of CMS is progressing well, though not without challenges, towards the goal of being ready for collisions in the second half of 2007. The overall layout of CMS is shown in Fig. 2-2. The core of CMS sits a 13-m-long, 5.9 m inner diameter superconducting solenoid, providing magnetic field up to 4 tesla. There are 4 sub-detector sets in CMS. The most inner part is occupied by tracking system composed of silicon pixel and strips. Behind the tracker, there sits the electromagnetic calorimeter(ECAL), and the hadron calorimeter(HCAL). At exterior most of the CMS, the muon chambers are arranged in this part. Due to the muon chambers are outside the magnet, there are layers of steel serve as return yoke in between each set of muon chambers. The overall dimensions of the CMS detector are a length of 21.6 m, a diameter of 14.6 m and a total weight of 12500 tons.

2.2.1 Coordinate in CMS

The coordinate system adopted by CMS has the origin centered at the nominal collision point inside the experiment, the y-axis pointing vertically upward, and the x-axis pointing radially inward toward the center of the LHC. Thus, the z-axis points along the counter-clockwise beam direction. The azimuthal angle ϕ is measured from the x-axis in the x-y plane. The polar angle θ is measured from the z-axis. Pseudorapidity is defined as $\eta = -\ln \tan(\theta/2)$. Thus, the momentum and energy measured transverse to the beam direction, denoted by p_T and E_T , respectively, are computed

CMS Detector

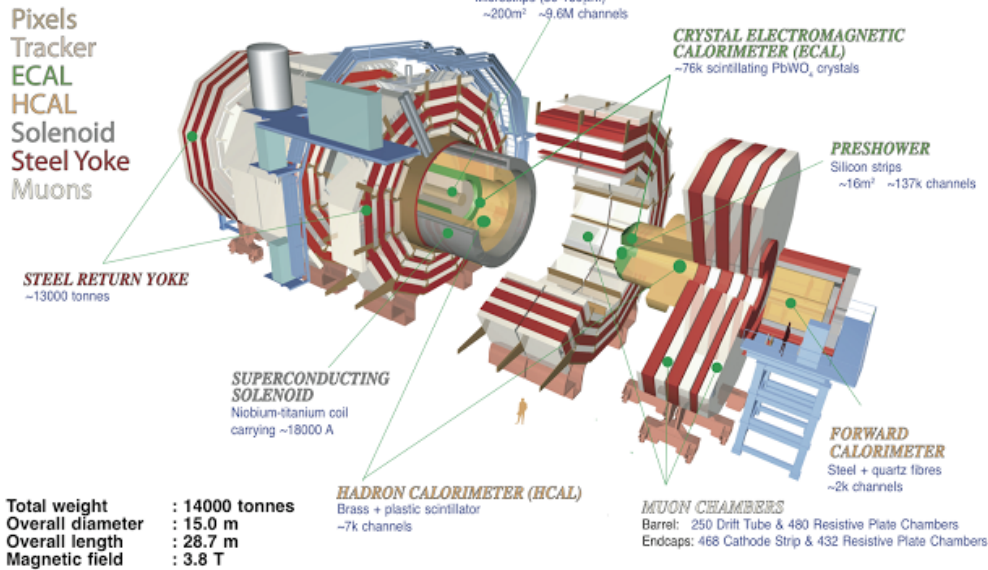


Figure 2-2: The Compact Muon Solenoid.

from the x and y components. The imbalance of energy measured in the transverse plane is denoted by E_T^{miss} .

2.2.2 Superconduction solenoid

CMS chose a large superconducting solenoid, the parameters of which are given in Tab 2.1. A large bending power can be obtained for a modestly-sized solenoid, albeit a high-field superconducting one, as the bending starts at the primary vertex. A favorable length to radius ratio is necessary to ensure good momentum resolution in the forward region as well.

The main features of the CMS solenoid are the use of a high-purity aluminium-stabilised conductor and indirect cooling (by thermosyphon), together with full epoxy impregnation. This technique was successfully used previously in the construction of the large solenoids for ALEPH and DELPHI at LEP and for H1 at HERA. However, the large increase in magnetic field, Ampere-turns, forces and stored energy (2.7 GJ)

necessitated changes. In particular, a four-layer winding has been adopted using a novel conductor with a larger cross-section that can withstand an outward pressure (hoop stress) of 64 atmospheres. The conductor carries a current of 20 kA and has a compound structure. The Rutherford-type cable is co-extruded with pure aluminium, which acts as a thermal stabiliser. This insert is then electron-beam-welded to 2 plates, made of a high-strength aluminium alloy, for the mechanical reinforcement. The overall conductor cross section is $64 \times 22 \text{ mm}^2$.

Field	4T
Inner Bore	5.9 m
Length	12.9 m
Number of Turns	2168
Current	19.5 kA
Stored energy	2.7 GJ
Hoop stress	64 atm

Table 2.1: Parameters of the CMS superconducting solenoid.

2.2.3 Tracking system

Tracking system is the first detector setup that the productions of collisions first contacted. This part of sub-detector trace the charged particles' trajectories without consuming their energy(at least as possible), helping physics to find out the vertex and momentum of each particle by linking the tracks to the collider's pipe and measuring the curves of particles under 4 T magnetic field.

The layout of the CMS tracker is shown in Fig. 2-3. The outer radius of the CMS tracker extends to nearly 110 cm, and its total length is approximately 540 cm. The tracker in CMS is made of silicon pixel and silicon strip. Close to the interaction vertex, the pixel detector stands here to improve the vertex resolution. Pixel detector consists of 3 barrel layers with 2 endcap disks on each side on them(Fig. 2-4). The 3 barrel layers are located at mean radii of 4.4 cm, 7.3 cm and 10.2 cm, and have a length of 53 cm. The 2 end disks, extending from 6 to 15 cm in radius, are placed on each side at $-z = 34.5 \text{ cm}$ and 46.5 cm . The spatial resolution is measured to be

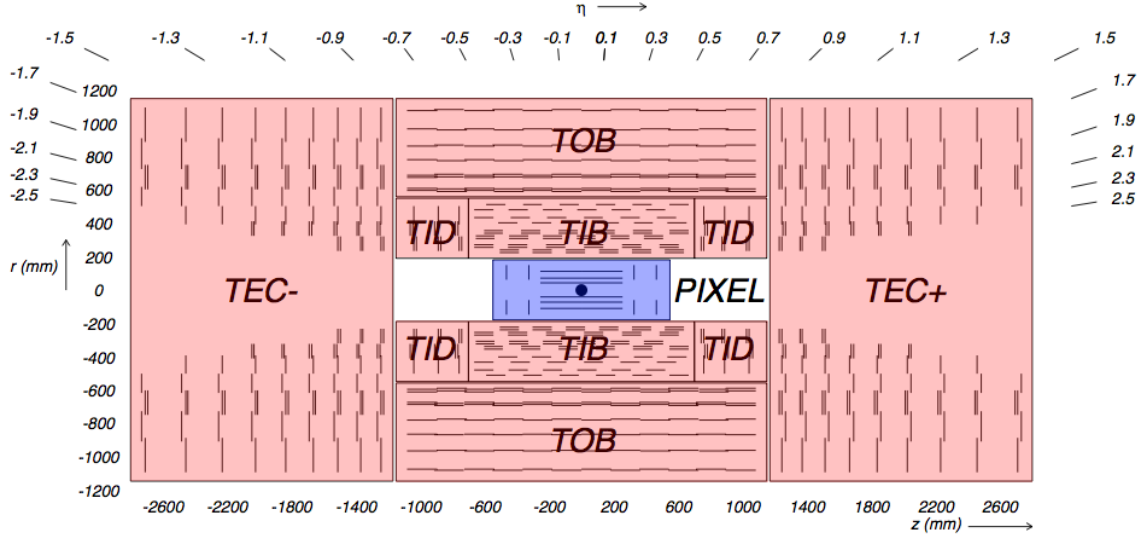


Figure 2-3: The tracker layout of CMS.

about $10 \mu\text{m}$ for the $r - \phi$ measurement and about $20 \mu\text{m}$ for the z measurement. Outside the pixel tracker, there comes the tracker composed of strips. The barrel part is separated into an Inner(TIB) and an Outer Barrel(TOB). In order to avoid excessively shallow track crossing angles, the Inner Barrel is shorter than the Outer Barrel. The TIB is made of 4 layers and covers up to $|z| < 65\text{cm}$, using silicon sensors with a thickness of $320 \mu\text{m}$ and a strip pitch which varies from 80 to 120 μm . The TOB comprises 6 layers with a half-length of $|z| < 110\text{cm}$. The endcaps are divided into the TEC (Tracker End Cap) and TID (Tracker Inner Disks). Each TEC comprises 9 disks that extend into the region $120\text{cm} < |z| < 280\text{cm}$, and each TID comprises 3 small disks that fit the gap between the TIB and the TEC. The entire silicon strip detector consists of almost 15400 modules, which will be mounted on carbon-fibre structures and housed inside a temperature controlled outer support tube. The operating temperature will be around -.

2.2.4 Electromagnetic calorimeter

High energy electrons and photons interact with matter mainly through bremsstrahlung and electron-positron pair production, depositing practically all their energy in an ad-

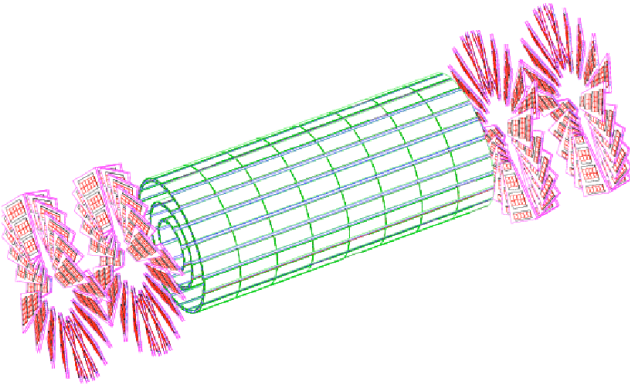


Figure 2-4: Pixel detector inside tracker.

equately designed calorimeter. Lead tungstate crystals (PbWO_4) have been chosen as the material for the CMS electromagnetic calorimeter (ECAL) for two reasons. Firstly, they are dense, so that an electromagnetic shower develops early and is very likely fully contained within a compact device. Secondly, they are fast scintillators, providing the possibility to detect the light emitted in the showering process. Silicon avalanche photo diodes (APD) have been selected for the light readout in the central region, since these devices can operate in a hostile radiation environment and high magnetic field.

The barrel section (EB) has an inner radius of 129 cm. It is structured as 36 identical supermodules, each covering half the barrel length and corresponding to a pseudorapidity interval of $0 < |\eta| < 1.479$. The endcaps (EE), at a distance of 314 cm from the vertex and covering a pseudorapidity range of $1.479 < |\eta| < 3.0$, are each consisting of semi-circular aluminium plates from which are cantilevered structural units of 5×5 crystals, known as supercrystals. A preshower device is placed in front of the crystal calorimeter over much of the endcap pseudorapidity range. The active elements of this device are 2 planes of silicon strip detectors, with a pitch of 1.9 mm, which lie behind disks of lead absorber at depths of $2 X_0$ and $3 X_0$. Beam tests have shown that the energy resolution of ECAL modules is excellent.

2.2.5 Hadron calorimeter

Hadrons such as protons, neutrons, pions or Kaons are strongly interacting particles, which feel the force that binds nuclei together. Like for electrons or photons their energy and position can be measured in a calorimeter. Hadronic showers start to develop later and have larger longitudinal and lateral dimensions than electromagnetic ones. The HCAL is made of alternating plates of brass and plastic scintillator read out through wavelength shifting optical fibres by photosensors in the barrel and endcap regions. The photosensors are hybrid photodiodes, which consist of a fibre-optic entrance window onto which a photocathode is deposited, followed by a gap of several millimeters over which a large applied electric field accelerates photoelectrons onto a silicon diode target. The very forward part of HCAL, the HF located at both sides of the detector, has steel absorber plates sampled by quartz fibres due to their good radiation tolerance.

2.2.6 Muon chamber

In order to detect a passing muon, three different types of muon chambers form a system consisting of drift tube (DT) chambers in the barrel, cathode strip chambers (CSC) in the endcaps and resistive plate chambers (RPC) glued to the DT and CSC chambers. Four layers, also called stations, of DT/RPC and CSC/RPC chambers are embedded into the iron yoke in order to make up a redundant system that can guarantee optimal performance both in the reconstruction of tracks and in triggering. The layout of one quarter of the CMS muon system for initial low luminosity running is shown in Fig. 2-5. In the Muon Barrel (MB) region, 4 stations of detectors are arranged in cylinders interleaved with the iron yoke. In each of the endcaps, the CSCs and RPCs are arranged in 4 disks perpendicular to the beam, and in concentric rings, 3 rings in the innermost station, and 2 in the others.

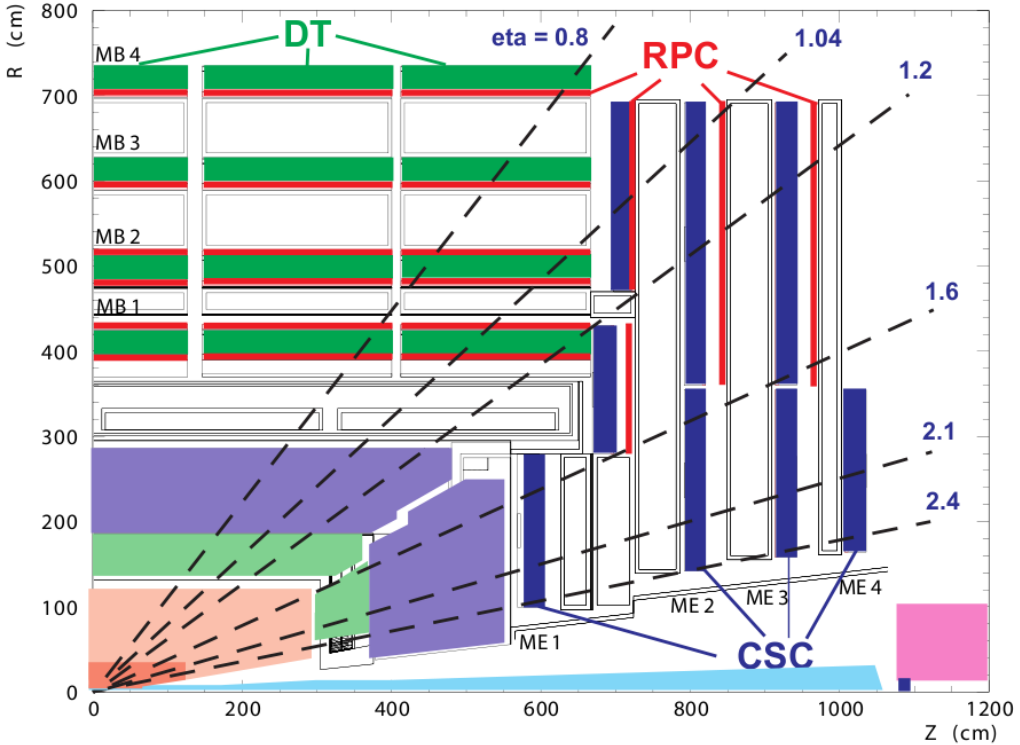


Figure 2-5: The layout of muon chambers in CMS.

Drift tube chamber

The drift tube (DT) system measures muon positions in the barrel part of the detector. Each 4-cm-wide tube contains a stretched wire within a gas volume. When a muon or any charged particle passes through the volume it knocks electrons off the atoms of the gas. These follow the electric field ending up at the positively-charged wire. The Barrel Detector consists of 250 chambers organized in 4 layers (stations labeled MB1, MB2, MB3 and MB4 with the last being the outermost) inside the magnet return yoke, at radii of approximately 4.0, 4.9, 5.9 and 7.0 m from the beam axis. Chambers in different stations are staggered so that a high- p_T muon produced near a sector boundary crosses at least 3 out of the 4 stations. There are 12 chambers in each of the 3 inner layers. In the 4th layer, the top and bottom sectors host 2 chambers each, thus leading to a total of 14 chambers per wheel in this outermost layer. The maximum drift length is 2.0 cm and the single-point resolution is about 200 μ m. Each station is designed to give a muon vector in space, with a ϕ precision

better than $100\ \mu m$ in position and approximately 1 mrad in direction.

Each DT chamber has 1 or 2 RPCs coupled to it before installation, depending on the station. In stations MB1 and MB2, each package consists of 1 DT chamber sandwiched between 2 RPCs. In stations MB3 and MB4, each package comprises 1 DT chamber and 1 RPC, which is placed on the innermost side of the station. A high- p_T muon thus crosses up to 6 RPCs and 4 DT chambers, producing up to 44 measured points in the DT system from which a muon-track candidate can be built.

Cathode strip chamber

The Muon Endcap (ME) system comprises 468 CSCs in the 2 endcaps. Each CSC is trapezoidal in shape and consists of 6 gas gaps, each gap having a plane of radial cathode strips and a plane of anode wires running almost perpendicularly to the strips. All CSCs except those in the third ring of the first endcap disk (ME1/3) are overlapped in phi to avoid gaps in the muon acceptance. The gas ionization and subsequent electron avalanche caused by a charged particle traversing each plane of a chamber produces a charge on the anode wire and an image charge on a group of cathode strips. The signal on the wires is fast and is used in the Level-1 Trigger. However, it leads to a coarser position resolution. A precise position measurement is made by determining the centre-of-gravity of the charge distribution induced on the cathode strips. The spatial resolution provided by each chamber from the strips is typically about $200\ \mu m$ ($100\ \mu m$ for ME1/1). The angular resolution in ϕ is of order 10 mrad.

Resistive plate chamber

Resistive plate chambers (RPC) are fast gaseous detectors that provide a muon trigger system parallel with those of the DTs and CSCs. RPCs consist of two parallel plates, a positively-charged anode and a negatively-charged cathode, both made of a very high resistivity plastic material and separated by a gas volume. When a muon passes through the chamber, electrons are knocked out of gas atoms. These electrons in turn

hit other atoms causing an avalanche of electrons. The electrodes are transparent to the signal (the electrons), which are instead picked up by external metallic strips after a small but precise time delay. The pattern of hit strips gives a quick measure of the muon momentum, which is then used by the trigger to make immediate decisions about whether the data are worth keeping. RPCs combine a good spatial resolution with a time resolution of just 1 ns.

2.3 Trigger system

The LHC accelerator will provide proton-proton and heavy-ion collisions at high interaction rates. The bunch crossing interval for protons is 25 ns. Depending on luminosity, several proton-proton interactions occur at each crossing of the beams. At the nominal design luminosity of $10^{-34} \text{ cm}^{-2} \text{ s}^{-1}$ approximately 20 proton-proton events are superimposed, and the interaction rate is of the order of 1 GHz. Since it is impossible to store and process the large amount of information. About 1 MB of zero-suppressed data per event associated with the resulting high number of events, a drastic rate reduction has to be achieved. This task is performed by the trigger system, which is the start of the physics event selection process. In CMS the input rate is reduced in two steps called Level-1 Trigger(L1T) and High-Level Trigger(HLT), respectively. The structure of the trigger system is shown in Fig. 2-6.

Level-1 trigger

The size of the LHC detectors and the underground caverns imposes a minimum transit time for signals from the front-end electronics to reach the services cavern housing the Level-1 trigger logic and return back to the detector front-end electronics. The total time allocated for the transit and for reaching a decision to keep or discard data from a particular beam crossing is $3.2 \mu\text{s}$. During this time, the detector data must be held in buffers while trigger data is collected from the front-end electronics and decisions reached that discard a large fraction of events while retaining the small fraction of interactions of interest. Of the total latency, the time allocated to Level-1

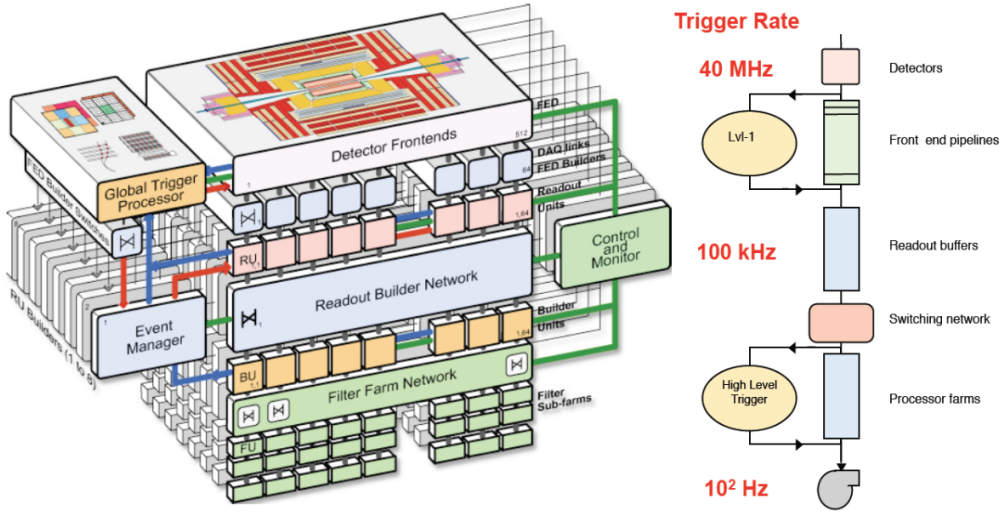


Figure 2-6: The trigger system in CMS.

trigger calculations is less than $1 \mu s$.

The Level-1 triggers involve the calorimetry and muon systems, as well as some correlation of information between these systems. The Level-1 decision is based on the presence of trigger primitive objects such as photons, electrons, muons, and jets above set E_T or p_T thresholds. It also employs global sums of E_T and E_T^{miss} . During the Level-1 decision-making period, all the high-resolution data is held in pipelined memories. Commodity computer processors make subsequent decisions using more detailed information from all of the detectors in more and more sophisticated algorithms that approach the quality of final reconstruction.

High level trigger

Through the event building “switch”, data from a given event are transferred to a processor. Each processor runs the same high-level trigger (HLT) software code to reduce the Level-1 output rate of 100 kHz to 100 Hz for mass storage. Various strategies guide the development of the HLT code. Rather than reconstruct all possible objects in an event, whenever possible only those objects and regions of the detector that are actually needed are reconstructed.

Chapter 3

Analysis Procedures

In this chapter, the procedures of the search of excited leptons in $2e2\mu$ final state is described. The data and Monte-Carlo(MC) samples used in this analysis, search strategies, and the final selected yields will be reported. Some information of 4μ and $4e$ channel will be referred as well in order to provide a complete picture of this search, although this thesis mainly focuses on $2e2\mu$ channels.

3.1 Data and Monte-Carlo samples

3.1.1 Data samples

In this analysis, the full CMS data collected in 2012 is used, corresponding to the integrated luminosity of $19.7 \pm 0.5 \text{ fb}^{-1}$ [15]. The data were recorded at a centre-of-mass energy of $\sqrt{s} = 8 \text{ TeV}$ and analyzed with the CMSSW53X software. There are 4 channels and 3 datasets used in this analysis. $\mu\mu^* \rightarrow 4\mu$ uses the double muon dataset. $\mu\mu^* \rightarrow 2\mu 2e$, and $ee^* \rightarrow 2e2\mu$ relies on muon-photon dataset. $ee^* \rightarrow 4e$ rides on double electron dataset. The full dataset names are listed in Tab. 3.1. The name of dataset reveals the information of the trigger selection, which will be described in next section.

CMS Run Range	Dataset Name
190456 - 193621	/DoubleMu/Run2012A-22Jan2013-v1/AOD /DoubleElectron/Run2012A-22Jan2013-v1/AOD /MuEG/Run2012A-22Jan2013-v1/AOD
193833 - 196531	/DoubleMuParked/Run2012B-22Jan2013-v1/AOD /DoubleElectron/Run2012B-22Jan2013-v1/AOD /MuEG/Run2012B-22Jan2013-v1/AOD
198022 - 203742	/DoubleMuParked/Run2012C-22Jan2013-v1/AOD /DoubleElectron/Run2012C-22Jan2013-v1/AOD /MuEG/Run2012C-22Jan2013-v1/AOD
203777 - 208686	/DoubleMuParked/Run2012D-22Jan2013-v1/AOD /DoubleElectron/Run2012D-22Jan2013-v1/AOD /MuEG/Run2012D-22Jan2013-v1/AOD

Table 3.1: Summary of the data samples used in this analysis

3.1.2 Monte Carlo samples

Tab. 3.2 and 3.3 summarize the information on Monte Carlo(MC) samples used for signals and backgrounds. The MC samples were processed with different generators and ran through a GEANT4 [16] detector simulation. For the signals, leading order(LO) cross sections with a k-factor for QCD corrections [1] are used. Cross sections show in Tab. 3.2 are calculated with $f = f' = 1$. For $f = -f' = -1$, where γ -mediated channel is forbidden, the cross sections are 3.5 times larger than $f = f' = 1$ case. Background samples use next-to-leading order(NLO) cross sections. Both of signal and background MC samples are produced with the Summer12 MC conditions. For the background, samples are the one officially produced with PYTHIA, MADGRAPH [17] and POWHEG [18] in CMS experiment.

The signal samples are produced with PYTHIA 8 [13] at $\Lambda = 10$ TeV. PYTHIA8 can only simulate the production via contact interaction and the decay via gauge interaction. The calculation of the PYTHIA8 cross section is done via

$$\sigma_{ll^* \rightarrow llZ \rightarrow 2l2l'}^{Pythia\,8} = \frac{\Gamma_Z \cdot \Gamma_{Z \rightarrow ll}}{\Gamma_Z + \Gamma_W + \Gamma_\gamma} \cdot \sigma_{ll^*}^{Pythia\,8} = \frac{\Gamma_Z \cdot \Gamma_{Z \rightarrow ll}}{\Gamma_G} \cdot \sigma_{ll^*}^{Pythia\,8} \quad (3.1)$$

where Γ_G is the decay width of all gauge interaction decays. However, it is possible

that the excited lepton decays via contact interaction instead of gauge interaction. In this case, the cross section calculated by Pythia 8 will be overestimated. The actual cross section of excited lepton decay via Z boson should have form

$$\sigma_{ll^*\rightarrow llZ\rightarrow 2l2l'} = \frac{\Gamma_Z \cdot \Gamma_{Z\rightarrow ll}}{\Gamma_G + \Gamma_{CI}} \cdot \sigma_{ll^*} \quad (3.2)$$

with the contact interaction decay width Γ_{CI} included. To get this cross section, the one given by Pythia 8 has to be scaled with the correction factor

$$c = \frac{\Gamma_G}{\Gamma_G + \Gamma_{CI}}. \quad (3.3)$$

This factor strongly depends on the ratio M_{l^*}/Λ . This is due to the different dependence of M_{l^*}/Λ in Γ_{CI} and Γ_G . Γ_{CI} is a function of $M_{l^*}^5/\Lambda^4$ while Γ_G is a function of $M_{l^*}^3/\Lambda^2$. This indicates that the contact interaction will be dominate as M_{l^*} approaches Λ . For example, for $\Lambda = 10$ TeV and $M_{l^*} = 200$ GeV, the factor $c = 0.993$ while for a mass of 2600 GeV, it decreases to $c = 0.538$. The lowest value of this factor is given at $M_{l^*} = \Lambda$ with $c = 0.07$. The importance of scaling down the cross section calculated by Pythia 8 is to give out a more conservative result of the search, avoiding an overestimated upper limit.

M_{l^*} (GeV)	cross section \times BR without CI decay (pb)	cross section \times incl. CI decay (pb)	k-factor	# events μ^*/e^*
200	$2.095 \cdot 10^{-4}$	$2.081 \cdot 10^{-4}$	1.296	8500 / 8500
400	$1.363 \cdot 10^{-4}$	$1.334 \cdot 10^{-4}$	1.290	10000 / 10000
600	$8.122 \cdot 10^{-5}$	$7.757 \cdot 10^{-5}$	1.282	10000 / 8000
800	$4.817 \cdot 10^{-5}$	$4.449 \cdot 10^{-5}$	1.273	9000 / 10000
1000	$2.844 \cdot 10^{-5}$	$2.520 \cdot 10^{-5}$	1.268	10000 / 10000
1200	$1.675 \cdot 10^{-5}$	$1.414 \cdot 10^{-5}$	1.265	8000 / 10000
1400	$9.786 \cdot 10^{-6}$	$7.826 \cdot 10^{-6}$	1.267	9000 / 10000
1600	$5.686 \cdot 10^{-6}$	$4.286 \cdot 10^{-6}$	1.272	10000 / 10000
1800	$3.286 \cdot 10^{-6}$	$2.325 \cdot 10^{-6}$	1.282	10000 / 10000
2000	$1.875 \cdot 10^{-6}$	$1.242 \cdot 10^{-6}$	1.295	10000 / 10000
2200	$1.062 \cdot 10^{-6}$	$6.569 \cdot 10^{-7}$	1.311	10000 / 10000
2400	$5.936 \cdot 10^{-7}$	$3.424 \cdot 10^{-7}$	1.329	10000 / 10000
2600	$3.280 \cdot 10^{-7}$	$1.763 \cdot 10^{-7}$	1.348(*)	10000 / 10000

Table 3.2: Summary of Monte Carlo signal samples, cross sections (LO), and k-factors used for $ll^* \rightarrow llZ \rightarrow 2l2l'$ ($l = e, \mu$ and $l' = e, \mu, \tau$) with $\Lambda = 10$ TeV and $f = f' = 1$.
(*) The k-factor for 2600 GeV was calculated by extrapolation [1].

3.2 Trigger

Three different triggers are used in this search. $\mu\mu^* \rightarrow \mu\mu Z \rightarrow 4\mu$ channel uses the double muon trigger with at least one 17 GeV muon and one 8 GeV muon, *HLT_Mu17_Mu8_v**. For $ee^* \rightarrow eeZ \rightarrow 4e$, the double electron trigger with at least one 17 GeV electron and one 8 GeV electron, *HLT_Ele17_Ele8_v**, is used. The two cross channels $\mu\mu^* \rightarrow \mu\mu Z \rightarrow 2\mu 2e$ and $ee^* \rightarrow eeZ \rightarrow 2e 2\mu$ use the muon-photon trigger with at least one muon and one photon excess 22 GeV, *HLT_Mu22_Photon22_**. The choice of the trigger in 4μ and $4e$ are pretty intuitive, but why is the muon-photon trigger used in the $2e2\mu$ channels? The reason is the muon-electron trigger is inefficient in the $\mu\mu^* \rightarrow \mu\mu Z \rightarrow 2\mu 2e$ channel due to the isolation requirement for electrons in trigger. In high mass signal regions, Z boson from μ^* decay may be highly boosted, it causes the electron pair decaying from boosted Z too close to each other, and furthermore is rejected by the isolation requirement of electron in trigger. Fortunately, an electron acts similarly to a photon in the electromagnetic calorimeter, every electron is also a photon in this stage of analysis. This character-

istic offers a great opportunity to use muon-photon trigger, which does not include isolation requirements on photon, instead of muon-electron trigger to avoid the issue of isolation requirement. The performance of different triggers as a function of excited lepton mass for both $2e2\mu$ channels are shown in Fig. 3-1. Though the muon-electron trigger is only inefficient in $\mu\mu^* \rightarrow 2\mu 2e$, for convenience, both channels are analyzed with the same muon-photon trigger. The muon-photon trigger efficiencies are close to one in both cases.

3.3 Object reconstruction and identification

3.3.1 Electron reconstruction

Electron is a particle that involves in various electroweak decays in the experiment. An electron in the CMS experiment leaves the footprint in tracker and deposits its entire energy in ECAL. Therefore, to reconstruct an electron, it's essential to find a brilliant way to match the information acquired in both of tracker and ECAL.

ECAL clustering

For electrons, which deposit their entire energy to several crystals in ECAL, clustering is an important step for energy reconstruction. For every single hit in ECAL from an electron or a photon, approximately 94% of energy is contained in 3×3 crystals, and 97% in 5×5 crystals. To form a basic cluster, crystals with $E_T > 1\text{GeV}$ are picked up as seeds. Then, starting from seed crystal, dominos of size 1×3 or 1×5 are created in $\eta - \phi$ plane. Energy of these dominos are then added up along ϕ direction if energy of a domino exceed 0.1 GeV threshold. However, a single energy cluster can not reconstruct the energy well enough for an electron or a photon in real world, which involves bremsstrahlung and conversion process.

During the flight through the detectors under strong magnetic field, each electron may create several photons due to bremsstrahlung along ϕ direction. To correctly reconstruct the energy of an electron, it is needed to take the energy of photons from

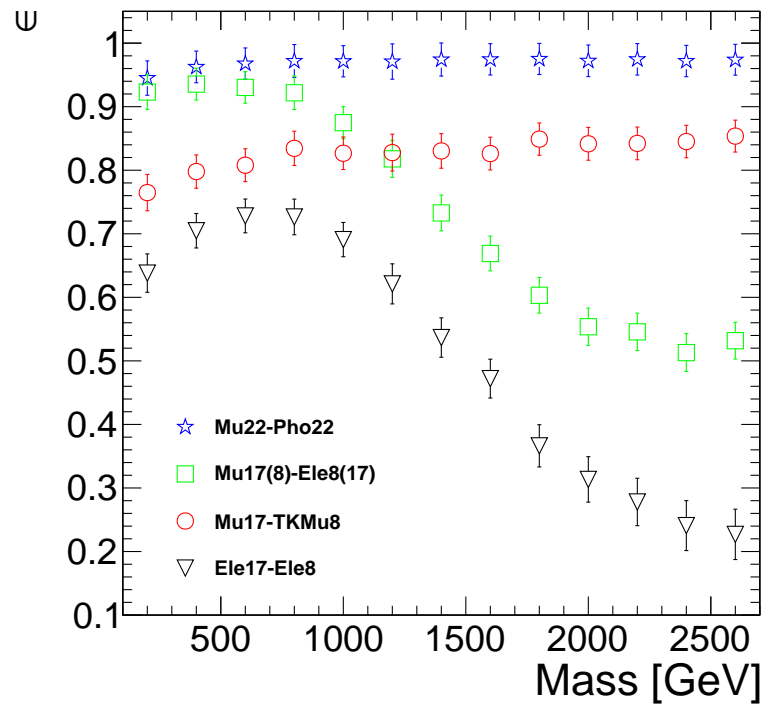
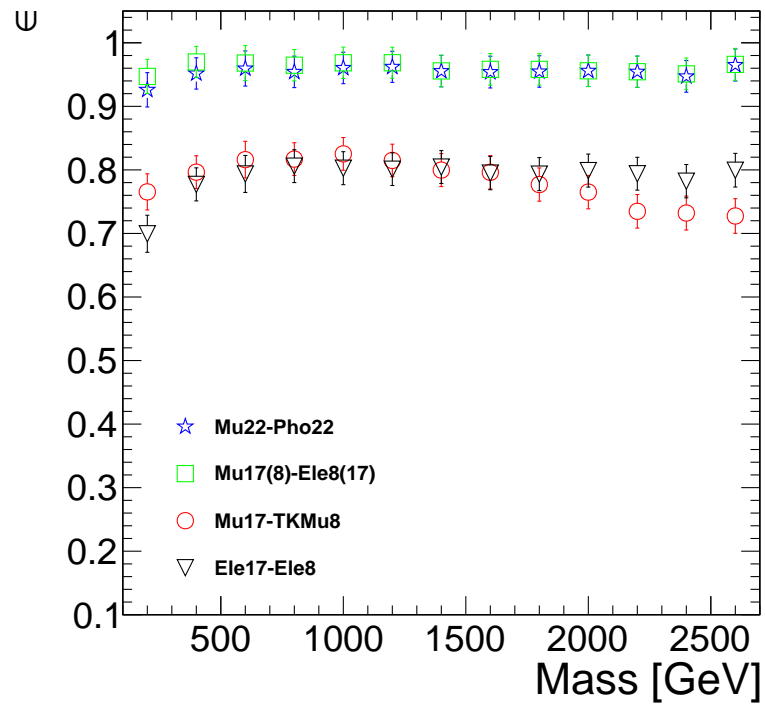


Figure 3-1: The comparison of different trigger efficiencies as a function of excited lepton mass for both $2e2\mu$ channels. Top: $ee^* \rightarrow 2e2\mu$ channel. Bottom: $\mu\mu^* \rightarrow 2\mu2e$ channel.

bremsstrahlung into account to form a larger cluster, called supercluster. The concept of superclustering is to collect the energy along the ϕ direction starting from the position of the seed crystal with a fixed η width. The technical details of the clustering can be found in [19].

Electron tracking

The track reconstruction in CMS experiment contains several steps. First, the hit on the pixel and the tracker should be reconstructed. The second step is to find the seed of tracks by matching at least 2 hits in pixel detector. The last step is to fit the trajectory starting from the seed [19, 20]. In general case, Kalman filter(KF) is used to fit the trajectory [21], but it is not suitable for electrons due to the relatively large energy loss in bremsstrahlung. Therefore, the Gaussian-sum filter(GSF) algorithm is developed to substitute the KF for electron reconstruction [20]. In GSF algorithm, the energy loss probability density function is constructed by multiple Gaussians instead of a single Gaussian as described in Bethe-Heitler model [22]. It turns out that GSF provide a better momentum resolution than KF, and the GSF algorithm is used in electron reconstruction [20]. Finally, the electrons are built by matching the supercluster to the GSF track. The reconstruction efficiency of electrons E_T greater than 20 GeV is generally above 95%(90%) in EB(EE) [23].

3.3.2 Electron identification

The high p_T electron selection used in this analysis (HEEP selection [24]) starts from a GSF electron on which kinematic, identification(ID) and isolation(Iso) cuts are applied. The major difference between HEEP selection and standard electron selection is the use of electron energy measurement. Later one is measured by the combination of tracker and Ecal information. However, under certain situations, one can discard the calorimeter energy completely (most likely in the crack region) and just use the track momentum, while calorimeter measurement is highly dominated in high p_T region. In this case, if the track is badly reconstructed, it might cause a low

p_T electron to become a high p_T one. To avoid this problem, HEEP selection always takes energy of the supercluster as the energy of an electron. The requirements used in electron selection are as follows.

- Kinematic requirements: Electrons with $E_T > 25$ GeV and $|\eta_{SC}| < 2.5$ but not within the transition region between EB and EE
- Is ECAL driven: Electrons should be reconstructed from an ECAL seed
- $\Delta\eta_{in}$: The difference in η between the track position measured in the inner tracker layers and the η of the supercluster
- $\Delta\phi_{in}$: The difference in ϕ between the track position measured in the inner tracker layers and the ϕ of the supercluster
- H/E: The ratio of the hadronic energy in a cone of radius 0.15 centred on the electron's position in the calorimeter to the electromagnetic energy of the electron's supercluster
- $\sigma_{i\eta i\eta}$: A measure of the spread in eta in units of crystals of the electrons energy in the 5x5 block centred on the seed crystal
- $E_{2\times 5}/E_{5\times 5}$: The maximum energy fraction of 2×5 crystal blocks(including seed crystal) in the 5×5 seed cluster
- $E_{1\times 5}/E_{5\times 5}$: The maximum energy fraction of 1×5 crystal blocks(including seed crystal) in the 5×5 seed cluster
- Inner layer lost hits: Number of lost hits in inner tracker
- d_{xy} : The distance between the electron track and the primary vertex in x-y plane
- Iso_{Trk} : The sum of tracks' p_T in a ΔR cone of 0.04 to 0.3 centered at electron position

- Iso_{Ecal} : The sum of E_T in a ΔR cone of 0.3 centered at electron position, excluding the inner cone of 3 crystals in Ecal
- Iso_{Hcal} : The sum of E_T in a ΔR cone of 0.15-0.3 centered at electron position in Hcal

The detail criteria of the selection are listed in Tab. 3.4. When the electrons decay from a highly boosted Z boson, they might get too closed to each other and fail the isolation requirement. Hence, the isolation is modified when ΔR between two electrons is less than 0.3 by subtracting the contribution from the other electron. This modification is the same as what is done in boosted Z analysis [25]. The data and MC match each other well for used ID and isolation. To make MC simulation more likely to realistic, a “scale factor” is applied to MC samples to correct the selection efficiency difference between data and MC. For electron scale factor, the official numbers calculated by HEEP group in CMS is applied [26] as shown in Tab. 3.5.

3.3.3 Muon reconstruction

Muon is an important object in CMS experiment. Even the name of the experiment contains the word “muon”. It is a kind of lepton just as electron and almost every electron-related process have also a muon-related channel. Muon leaves it’s footprints in tracker like electron, but it only deposits little of its energy in calorimeter. Nothing in CMS can stop muon’s flight as long as it isn’t super soft. It is the only kind of particle that can reach the outermost muon chamber and escape the detector to the outside world. This characteristic makes muon a highly recognized object in the experiment. The reconstruction efficiency is about 99% for the muon carries enough high momentum within detector coverage [27].

The reconstruction of muon track is first done independently by tracker(tracker track) and muon chamber(standalone track). There are two main approaches to match the track in tracker and muon chamber and bring out two different types of muon.

- Global muon: Starting from the reconstructed standalone track, the global muon algorithm finds a best tracker track to match the standalone track. Then, the global muon track is fitted by combining hits from the standalone track and tracker track using KF technique [21]. For high p_T muons up to 200 GeV, the global fit can improve the momentum resolution compared to the tracker-only fit [27].
- Tracker muon: A tracker muon is reconstructed by an opposite direction from a global muon. The tracker muon algorithm starts from the tracker track, and finds if there is at least one muon segment(muon segment is the short track form by the hits in DT or CSC. It's not a standalone track, which needs to match a muon "hits" in RPC) to match to the extrapolated track. It's more efficient than global fit for muon with only serveral GeV momentum, but for the muon used mostly in physics analysis, a muon is often reconstructed as a global muon and tracker muon simutaneously [27].

3.3.4 Muon identification

To select the muon, the "High p_T ID" from the muon POG is used [28]. The requirements used in muon selection are listed as follows:

- Kinematic requirements: Muons should have $p_T > 25$ GeV and $|\eta| < 2.4$
- Muon is a global muon
- Number of muon hits in the global track
- Muon stations: Number of muon segments in muon chamber
- d_{xy} : The distence between the muon track and the primary vertex in x-y plane
- d_z : The distence between the muon track and the primary vertex in z direction
- Number of pixel hits
- Number of tracker layers with hits

- $\Delta p_T/p_T$: The ratio of the transverse momentum error to its transverse momentum
- Iso_{TrkRel} : The relative isolation computed by the ratio of tracks p_T in a cone of ΔR 0.04-0.3 centered at muon tracks to muon's p_T

For the second muon of the Z decay(in $ee^* \rightarrow 2e2\mu$ channel), the ID is slightly modified due to an inefficiency in the global muon reconstruction for boosted objects decaying into two muons because they are close to each other. While one of the two muons is reconstructed as a global muon, the other one is only reconstructed as a tracker muon. This task leads to an inefficiency for the signal if we apply the high- p_T muon ID. To get around with this problem, the second muon is allowed to be a tracker muon instead of a global muon. Additionally, the requirement on the muon hits in the global tag is removed. The isolation of the two muons from the Z decay is also changed by removing the contribution of the other muon. Following statements are the modification to the high p_T muon ID for the muons coming from boosted Z decay.

- Muon doesn't have to be a global muon, but has to be a tracker muon
- Remove requirement for muon hits in global track
- Remove the contribution in Iso_{TrkRel} calculation of the other muon when two muons' tracks are within $\Delta R < 0.3$

The Tab. 3.6 summarized the muon selection criteria in this analysis.

Fig. 3-2 shows the isolation efficiency of the different lepton pairs for muons and for electrons. To account for the differences between the MC and data efficiencies, the scale factors for the ID and isolation criteria are applied [29–32]. The official numbers from the muon POG as shown in Tab.3.7-3.8 are applied on the muons pass the unmodified muon ID and isolation. For the muons that pass the modified selection criteria, the numbers calculated from the $X \rightarrow ZZ \rightarrow 2q2l$ group [33] in Tab. 3.9 are applied because they used the same modifications as this analysis. The errors in the tables are statistical uncertainties, systematic uncertainties will be discussed in Sec. 3.5. The two cases to use the modified scale factors are:

1. Muon passes the standard(global) high- p_T ID leg with the modified isolation
2. Muon passed the modified(tracker) high- p_T ID leg with the modified isolation

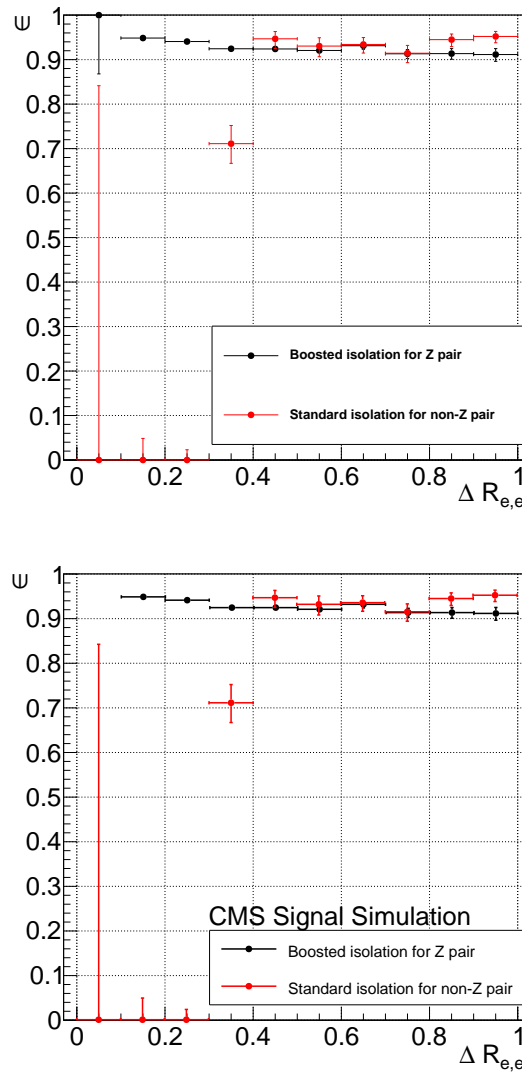


Figure 3-2: Efficiency of the isolation cut as a function of ΔR for electrons (top) and muons (bottom) for the non-Z pair with standard ID and the Z pair with boosted Z ID.

Process	Dataset Name	Cross section (pb)
$q\bar{q} \rightarrow ZZ \rightarrow 4e$	/ZZTo4e_8TeV - powheg - pythia6	0.07691
$q\bar{q} \rightarrow ZZ \rightarrow 4\mu$	/ZZTo4mu_8TeV - powheg - pythia6	0.07691
$q\bar{q} \rightarrow ZZ \rightarrow 4\tau$	/ZZTo4tau_8TeV - powheg - pythia6	0.07691
$q\bar{q} \rightarrow ZZ \rightarrow 2e2\mu$	/ZZTo2e2mu_8TeV - powheg - pythia6	0.1767
$q\bar{q} \rightarrow ZZ \rightarrow 2e2\tau$	/ZZTo2e2tau_8TeV - powheg - pythia6	0.1767
$q\bar{q} \rightarrow ZZ \rightarrow 2\mu2\tau$	/ZZTo2mu2tau_8TeV - powheg - pythia6	0.1767
$gg \rightarrow ZZ \rightarrow 2l2l'$	/GluGluToZZTo2L2L_8TeV - gg2zz - pythia6	0.01203
$gg \rightarrow ZZ \rightarrow 4l$	/GluGluToZZTo4L_8TeV - gg2zz - pythia6	0.0048
$WZ \rightarrow 3l\nu$	/WZJetsTo3LNu_TuneZ2_8TeV - madgraph - tauola	1.057
$WZ \rightarrow 2l2q$	/WZJetsTo2L2Q_TuneZ2star_8TeV - madgraph - tauola	1.755
ttZ	/TTZJets_8TeV - madgraph_v2	0.208
ttW	/TTWJets_8TeV - madgraph	0.232
$tt\gamma$	/TTGJets_8TeV - madgraph	2.17
$WW\bar{W}$	/TTWWJets_8TeV - madgraph	0.002
WWG	/WWGJets_8TeV - madgraph	1.44
WWZ	/WWZNuGstar_Jets_8TeV - madgraph	0.0633
WZZ	/WZZNoGstar_Jets_8TeV - madgraph	0.0197
ZZZ	/ZZZNuGstar_Jets_8TeV - madgraph	0.0046

Table 3.3: Summary of the used Monte Carlo background samples with the corresponding cross section in NLO.

Variable	Barrel	Endcap
E_T	$> 25 \text{ GeV}$	$> 25 \text{ GeV}$
$ \eta_{SC} $	$ \eta_{SC} < 1.442$	$1.56 < \eta_{SC} < 2.5$
Is Ecal Driven	yes	yes
$ \Delta\eta_{in} $	< 0.005	< 0.007
$ \Delta\phi_{in} $	< 0.06	< 0.06
H/E	< 0.05	< 0.05
$\sigma_{inj\eta}$	-	< 0.03
$E^{2\times 5}/E^{5\times 5}$	> 0.94 or $E^{1\times 5}/E^{5\times 5} > 0.83$	-
Inner Layer Lost Hits	$<= 1$	$<= 1$
$ d_{xy} $	$< 0.02 \text{ cm}$	$< 0.05 \text{ cm}$
$Iso_{Ecal+Hcal}$	$< 2 + 0.03E_T + 0.28\rho \text{ GeV}$	$< 2.5 + 0.28\rho \text{ GeV}$ for $E_T < 50 \text{ GeV}$ $< 2.5 + 0.03(E_T - 50) + 0.28\rho \text{ GeV}$ others
Iso_{Trk}	$< 5 \text{ GeV}$	$< 5 \text{ GeV}$

Table 3.4: HEEP electron ID

	$E_T < 100 \text{ GeV}$	$E_T > 100 \text{ GeV}$
$0 < \eta < 1.4442$	0.997 ± 0.000	0.985 ± 0.002
$1.4442 < \eta < 1.566$	0.979 ± 0.000	0.981 ± 0.006

Table 3.5: Scale factors for HEEP electron selection from HEEP group

Variable	Standard	Modified
p_T	$> 25 \text{ GeV}$	$> 25 \text{ GeV}$
$ \eta $	$ \eta < 2.4$	$ \eta < 2.4$
Muon type	Global muon	Tracker muon
Muon hits in global track	$>= 1$	-
Muon stations	$>= 2$	$>= 2$
d_{xy}	$< 0.2 \text{ cm}$	$< 0.2 \text{ cm}$
d_z	$< 0.5 \text{ cm}$	$< 0.5 \text{ cm}$
Pixel hits	$>= 1$	$>= 1$
Tracker layers	$>= 6$	$>= 6$
$\Delta p_T/p_T$	< 0.3	< 0.3
Iso_{TrkRel}	< 0.1	< 0.1

Table 3.6: High pT muon ID

	$p_T > 20$ GeV	$p_T > 45$ GeV
$0 < \eta < 0.9$	0.9930 ± 0.0002	0.9900 ± 0.0003
$0.9 < \eta < 1.2$	0.9942 ± 0.0003	0.9923 ± 0.0006
$1.2 < \eta < 2.1$	0.9968 ± 0.0002	0.9949 ± 0.0004
$2.1 < \eta < 2.4$	0.9963 ± 0.0006	0.9923 ± 0.0012

Table 3.7: Scale factors for high- p_T muon ID from MUO-POG

	$p_T > 20$ GeV	$p_T > 45$ GeV
$0 < \eta < 0.9$	1.0001 ± 0.0001	0.9996 ± 0.0001
$0.9 < \eta < 1.2$	1.0006 ± 0.0001	0.9994 ± 0.0001
$1.2 < \eta < 2.1$	1.0006 ± 0.0001	0.9997 ± 0.0001
$2.1 < \eta < 2.4$	1.0005 ± 0.0001	0.9997 ± 0.0001

Table 3.8: Scale factors for $\text{TkRelIso} < 0.1$ from MUO-POG

$ \eta $ bin	p_T (GeV)	GlobalID*ISO	TrackerID*ISO
$0 < \eta < 0.9$	20-40	0.9972 ± 0.0004	0.9989 ± 0.0004
	40-60	0.9948 ± 0.0003	0.9973 ± 0.0003
	60-80	1.0018 ± 0.0011	1.0029 ± 0.0010
	80-100	1.0076 ± 0.0025	1.0096 ± 0.0023
	100-500	1.0068 ± 0.0039	1.0075 ± 0.0037
$0.9 < \eta < 1.2$	20-40	0.9971 ± 0.0007	0.9988 ± 0.0007
	40-60	0.9963 ± 0.0005	0.9985 ± 0.0005
	60-80	1.0014 ± 0.0022	1.0028 ± 0.0021
	80-100	1.0060 ± 0.0049	1.0060 ± 0.0047
	100-500	1.0058 ± 0.0080	1.0050 ± 0.0077
$1.2 < \eta < 2.1$	20-40	1.0001 ± 0.0004	0.9999 ± 0.0005
	40-60	0.9982 ± 0.0004	0.9985 ± 0.0004
	60-80	1.0039 ± 0.0017	1.0039 ± 0.0016
	80-100	1.0129 ± 0.0039	1.0081 ± 0.0036
	100-500	1.0185 ± 0.0065	1.0180 ± 0.0063
$2.1 < \eta < 2.4$	20-40	1.0015 ± 0.0030	1.0028 ± 0.0009
	40-60	0.9955 ± 0.0012	0.9985 ± 0.0009
	60-80	0.9929 ± 0.0071	0.9927 ± 0.0024
	80-100	0.9834 ± 0.0092	0.9839 ± 0.0082
	100-500	1.0438 ± 0.0160	1.0083 ± 0.0099

Table 3.9: Scale factors used for the modified muon ID and isolation, taken from $X \rightarrow ZZ \rightarrow qql\bar{l}$ Analysis Note.

3.3.5 Pileup Reweighting

The Monte Carlo samples are generated with a distribution for the number of pileup interactions in order to roughly match the conditions in data [34]. However, there are differences between the pileup conditions in data and MC. Therefore, the pileup reweighting to MC samples is needed to account for the difference of pileup condition between data and MC. The Fig. 3-3 shows the number of vertices after pileup reweighting. By applying a proper weight to each MC event according to data's pileup distribution, the MC samples can describes the data better.

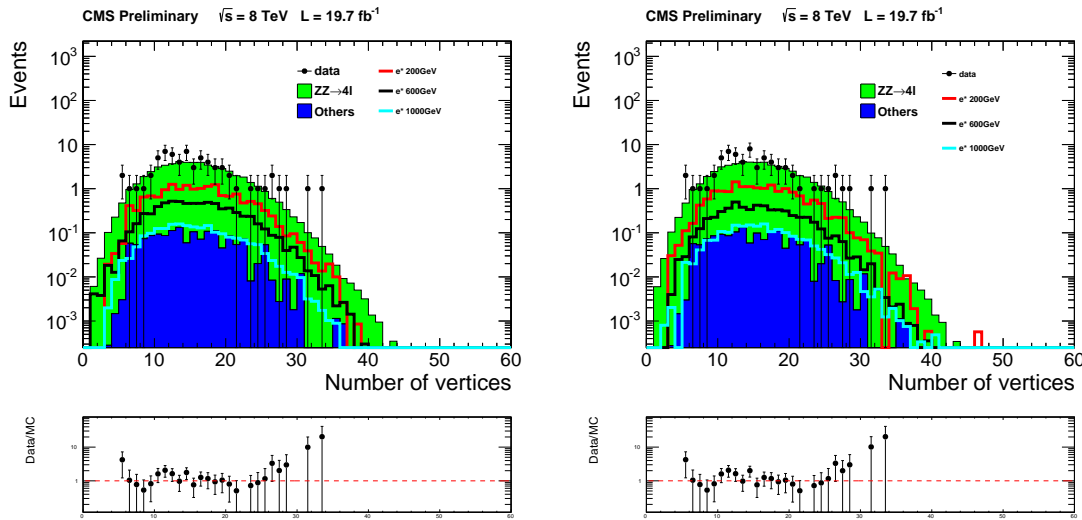


Figure 3-3: Number of Vertices distribution after PileUp reweighting for $\mu\mu^* \rightarrow \mu\mu Z \rightarrow 2\mu 2e$ (left), and $ee^* \rightarrow eeZ \rightarrow 2e 2\mu$ (right).

3.4 Event selection

In this section, the analysis strategy and background estimation are described. Comparison between data, signal, and background is done in this section as well. Furthermore, the most important part of this analysis, the mass spectrum of the reconstructed excited lepton is shown in the end of this section.

3.4.1 Analysis strategy

Following steps are applied for event selection:

- **Event cleaning:** no beam scraping events and at least one good vertex.
- **Trigger selection:** Use the triggers which were described in section 3.2
- **Muon selection:**
 - Selected muons have to satisfy the Exotica muon ID, as described in section 3.3.4. One muon has to satisfy the modified ID for the boosted Z signature.
 - All muons should have a $p_T > 25$ GeV and $|\eta| < 2.4$
 - Two muons which are not from the Z decay have to pass the isolation requirement and the two muons from the boosted Z decay have to pass the modified isolation requirement
- **Electron selection:**
 - Selected electron have to satisfy the HEEP v4.1 electron ID, as described in section 3.3.2.
 - All electrons should have a $p_T > 25$ GeV and $|\eta| < 2.5$ and not within $1.442 < |\eta| < 1.56$
 - The two electron from the boosted Z have to pass the modified electron isolation.
- **Number of leptons:** Require at least 2 electrons and 2 muons in every events

- **Z selection:** One lepton pair is expected to be produced by a Z boson decay. In $\mu\mu^* \rightarrow 2\mu 2e$ the electron pair comes from the Z decay and for $ee^* \rightarrow 2e 2\mu$ the muon pair comes from the Z decay. For the events with more than 2 possible candidates to reconstruct Z boson, the lepton pair with invariant mass closest to M_Z is choosed. An invariant mass cut of $M_{l_{Z_1}, l_{Z_2}} > 60$ GeV is applied to reduce the background which can raise two leptons without Z boson decay.
- **Z veto** For the leptons which are not selected to reconstruct Z, they are paired to form a non-Z lepton pair. In $\mu\mu^* \rightarrow 2\mu 2e$ the muons come from pair production and excited muon decay and for $ee^* \rightarrow 2e 2\mu$ the electrons come from pair production and excited electron decay. Two leptons with highest transverse momentum are selected if there are more than two possible candidates. The invariant mass of non-Z pair is required to be greater than 106 GeV. This Z-veto criteria can significantly reduce the main background, $ZZ \rightarrow 4l$, in this study.
- **Final selection:** This step define the final signal region in limit setting. The signal region is selected in the maximum-minimum three lepton invariant mass plane. The maximum and minimum invariant mass is reconstructed by the reconstructed Z and the two remaining leptons one by one. Take $\mu\mu^* \rightarrow 2\mu 2e$ for example, the three body invariant mass is reconstruced by two electrons plus one muon at a time, the one with higher three body mass is denoted as the maximum three body invariant mass, where as the other one is denoted as the minimum. The final signal region has an inverted L shape, which is shown in Fig. 4-3. The range of this selection will be revealed in the last chapter.

In this search, the analysis is divide to 3 stages. First, the events after lepton ID and Iso selection. In this stage, most of the background with 2 real muons and 2 real electrons still survive. The control plots of the whole analysis are taken in this stage. Second, the events after mass cuts(Z selection plus Z veto). Most of the backgrounds are removed in this stage, with most of the signals survived. The maximum and minimum three body invariant mass are reconstructed in this stage. Last, the events after final selection. In this stage, the final limit for excited lepton is set.

Tab. 3.10-3.11 show the event yields for each sample at each selecting stage. The background event yields in these tables are normalized to the luminosity while signal samples are presented by the percentage left at each stage. Fig. 3-4 shows the acceptance times efficiency of each mass point. By comparing the selecting acceptance times efficiency between all channels, including 4μ and $4e$ channels, the much higher result is observed in 4μ channel than others. This is found to be caused by the higher acceptance of muons' comparing to electrons' as shown in Fig. 3-5 and by the higher efficiency for the high- p_T muon ID in comparison to the HEEP 4.1 ID.

Sample	Acceptance	Trigger	ID and Isolation	Mass Cuts
$q\bar{q} \rightarrow ZZ \rightarrow 2e2\mu$	2.4%	2.4%	1.4%	0.1%
$q\bar{q} \rightarrow ZZ \rightarrow 2e2\tau$	0.0%	0.0%	0.0%	0.0%
$q\bar{q} \rightarrow ZZ \rightarrow 2\mu 2\tau$	0.0%	0.0%	0.0%	0.0%
$gg \rightarrow ZZ \rightarrow 2l2l'$	2.6%	2.5%	1.5%	0.0%
$gg \rightarrow ZZ \rightarrow 4l$	0.0%	0.0%	0.0%	0.0%
$WZ \rightarrow 3l\nu$	0.1%	0.1%	0.0%	0.0%
$t\bar{t}Z$	0.3%	0.2%	0.0%	0.0%
$t\bar{t}WW$	0.7%	0.5%	0.0%	0.0%
WWZ	0.2%	0.1%	0.0%	0.0%
WZZ	0.2%	0.1%	0.0%	0.0%
ZZZ	0.2%	0.2%	0.1%	0.0%
Total Background	0.4%	0.3%	0.1%	0.0%
200 GeV	50.4%	49.8%	29.1%	27.5%
1000 GeV	71.8%	71.2%	48.4%	47.0%
1800 GeV	75.7%	75.0%	49.5%	48.0%
2600 GeV	74.1%	73.3%	47.6%	46.4%

Table 3.10: Cut Flow Table for $\mu\mu^* \rightarrow \mu\mu Z \rightarrow 2\mu 2e$. The Acceptance step includes two electrons and two muons with $p_T > 25$ GeV in the geometrical acceptance, the ratio is calculated with respect to the full number of events (also those without two electrons and two muons).

Sample	Acceptance	Trigger	ID and Isolation	Mass Cuts
$q\bar{q} \rightarrow ZZ \rightarrow 2e2\mu$	2.4%	2.4%	1.4%	0.1%
$q\bar{q} \rightarrow ZZ \rightarrow 2e2\tau$	0.0%	0.0%	0.0%	0.0%
$q\bar{q} \rightarrow ZZ \rightarrow 2\mu 2\tau$	0.0%	0.0%	0.0%	0.0%
$q\bar{q} \rightarrow ZZ \rightarrow 4\tau$	0.0%	0.0%	0.0%	0.0%
$gg \rightarrow ZZ \rightarrow 2l2l'$	2.6%	2.5%	1.5%	0.0%
$gg \rightarrow ZZ \rightarrow 4l$	0.0%	0.0%	0.0%	0.0%
$WZ \rightarrow 3l\nu$	0.1%	0.1%	0.0%	0.0%
$t\bar{t}Z$	0.3%	0.2%	0.0%	0.0%
$t\bar{t}WW$	0.7%	0.5%	0.0%	0.0%
WWZ	0.2%	0.1%	0.0%	0.0%
WZZ	0.2%	0.1%	0.0%	0.0%
ZZZ	0.2%	0.2%	0.1%	0.0%
Total Background	0.3%	0.3%	0.1%	0.0%
200 GeV	49.0%	48.4%	30.6%	29.0%
1000 GeV	69.9%	68.9%	47.1%	46.4%
1800 GeV	77.5%	76.0%	52.1%	51.4%
2600 GeV	80.2%	77.8%	51.0%	50.0%

Table 3.11: Cut Flow Table for $ee^* \rightarrow eeZ \rightarrow 2e2\mu$. The Acceptance step includes two electrons and two muons with $p_T > 25$ GeV in the geometrical acceptance, the ratio is calculated with respect to the full number of events (also those without two electrons and two muons).

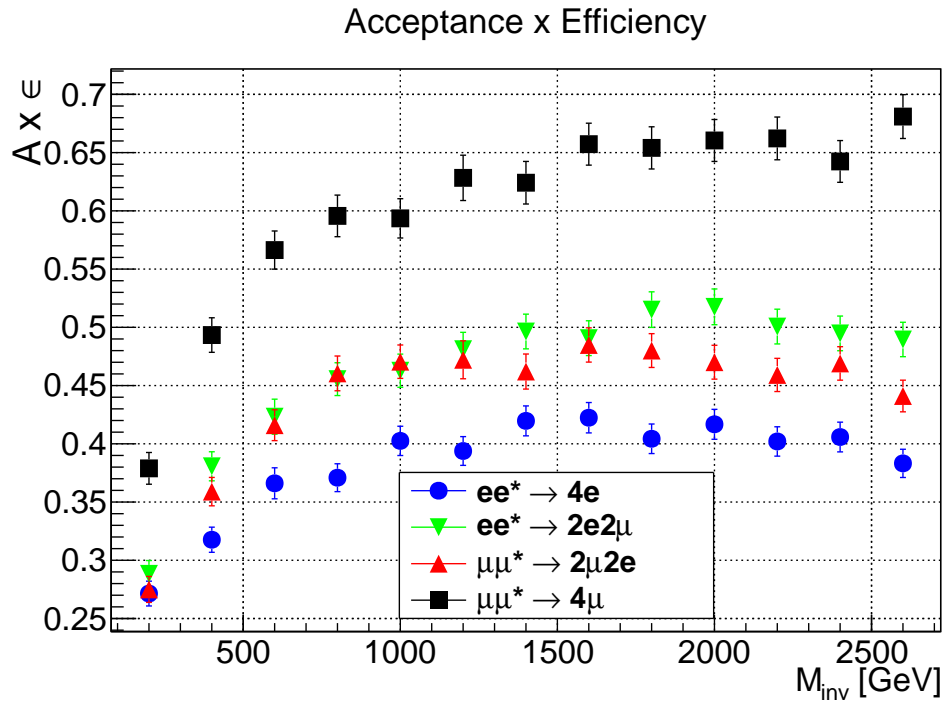


Figure 3-4: Total signal acceptance times efficiency ($A\epsilon$) for the all selection criteria before final selection for the various signal samples.

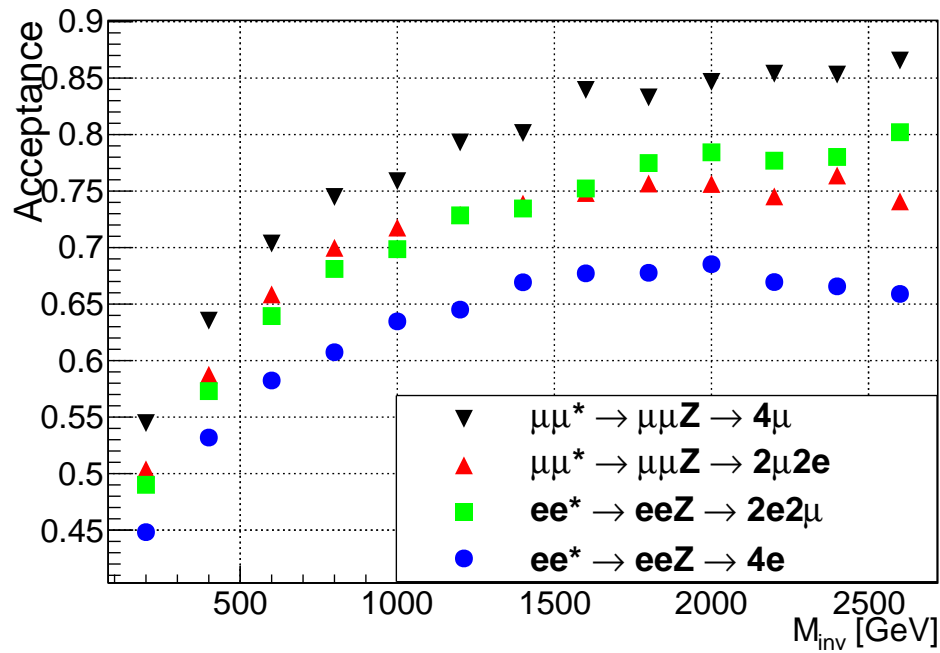


Figure 3-5: Geometrical acceptance for all channels as given in the legend, with 4 muons and 2e2mu in the final state.

3.4.2 Background estimation

After ID and isolation cuts

For a first comparison between data and background, the plots after applying the ID and isolation criteria for muons and electrons is shown. The plots in this section include scale factors for trigger, ID and isolation efficiencies and pileup re-weighting. Fig. 3-6 shows the distribution of the transverse momentum of the leptons. Fig. 3-7 shows the η distribution of the leptons while 3-8 shows the ϕ distribution. The distribution for the reconstructed Z is given in Fig. 3-9. Fig. 3-10 shows the invariant mass distribution of the non-Z lepton pair where the Z veto will be placed. As one can see from this plot, most signal events lays on the high invariant mass region beyond 106 GeV. Additionally, Fig. 3-11 and Fig. 3-12 show the invariant mass of all four leptons and the ΔR of the two muons from the Z decay. In all distributions, data and background are in same shape and agree with each other.

In Tab. 3.12 and Tab. 3.13 the contribution of each background can be seen for the two μ^* and the two e^* channels, and several sets of expected yield of signal at $\Lambda = M_{\ell^*}$ are provided as well. In the 4e channel, the agreement between data and MC is good. The 4μ channel has a small downward-fluctuation in data and the mixed channels have an upward-fluctuation in data. The fluctuation in the mixed channels has been investigated by changing the p_T cuts, using other ID (for example MVA electron ID) and doing comparisons to other analyses. The excess comes mainly from the region about 200 GeV in the four lepton invariant mass distribution. In this region, other analyses such as $H \rightarrow ZZ \rightarrow 4l$ (see Fig. 3-13) [35] do also observe an upward-fluctuation.

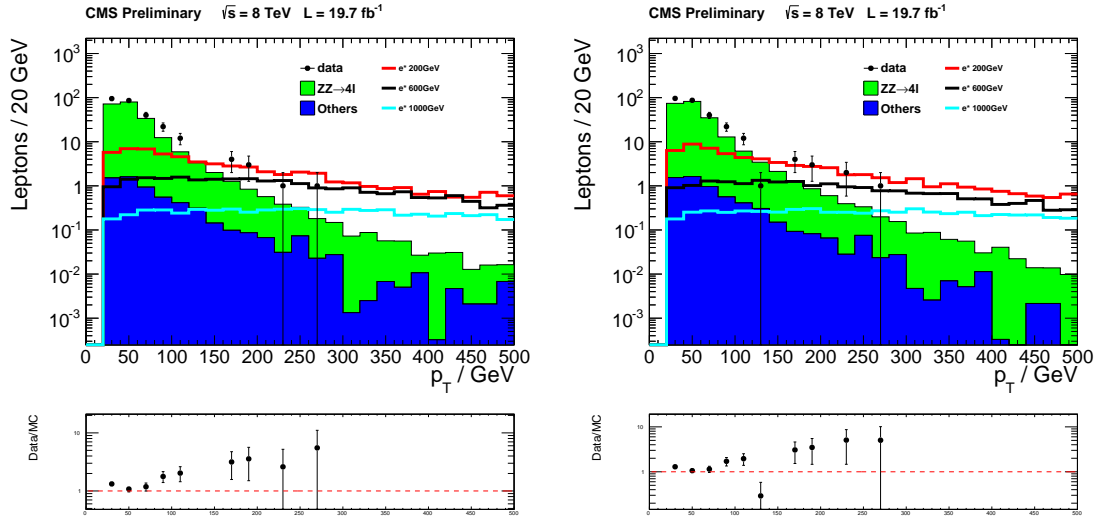


Figure 3-6: Lepton p_T before invariant mass cuts. Left: $\mu\mu^* \rightarrow 2\mu 2e$ channel, Right: $ee^* \rightarrow 2e 2\mu$ channel

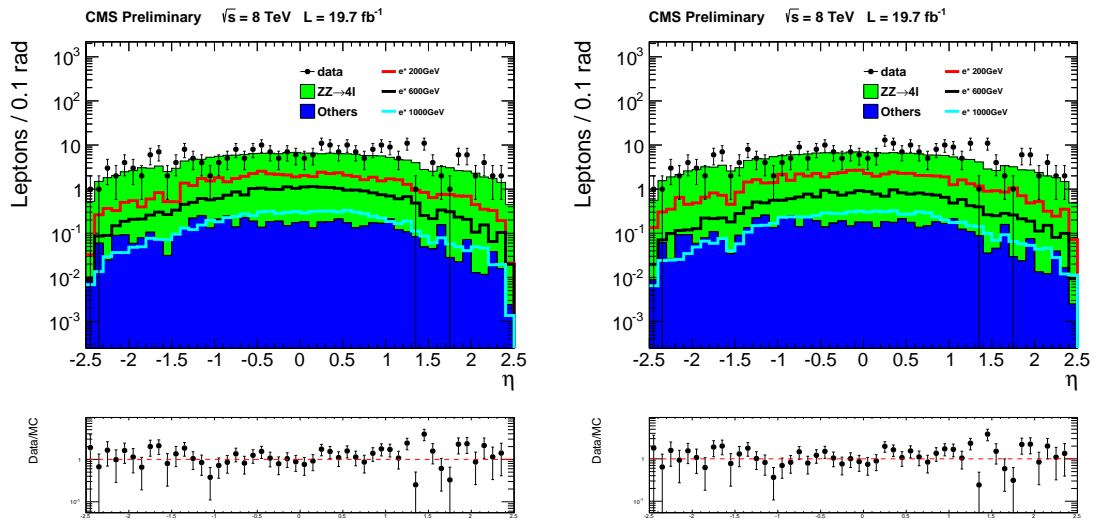


Figure 3-7: Lepton η before invariant mass cuts. Left: $\mu\mu^* \rightarrow 2\mu 2e$ channel, Right: $ee^* \rightarrow 2e 2\mu$ channel

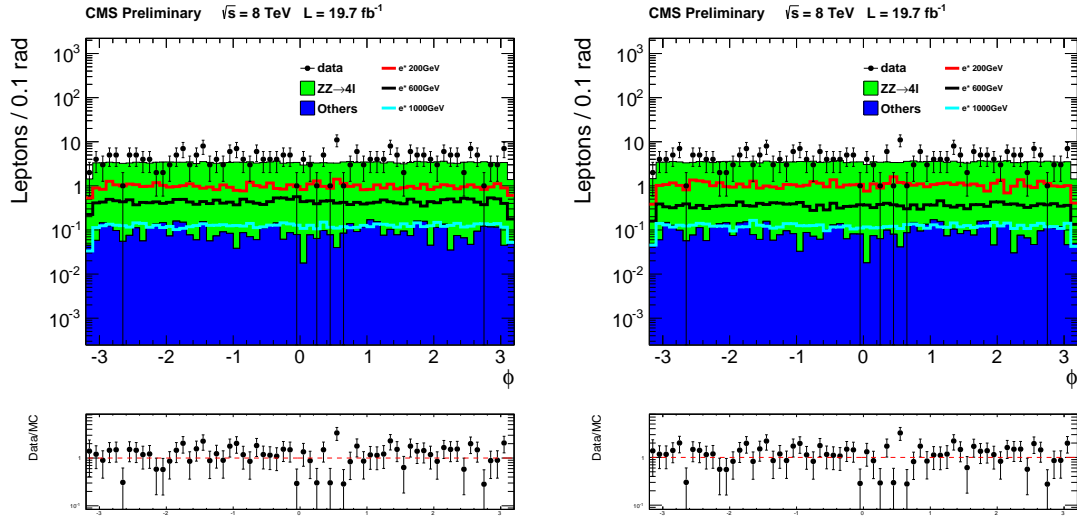


Figure 3-8: Lepton ϕ before invariant mass cuts. Left: $\mu\mu^* \rightarrow 2\mu 2e$ channel, Right: $ee^* \rightarrow 2e 2\mu$ channel

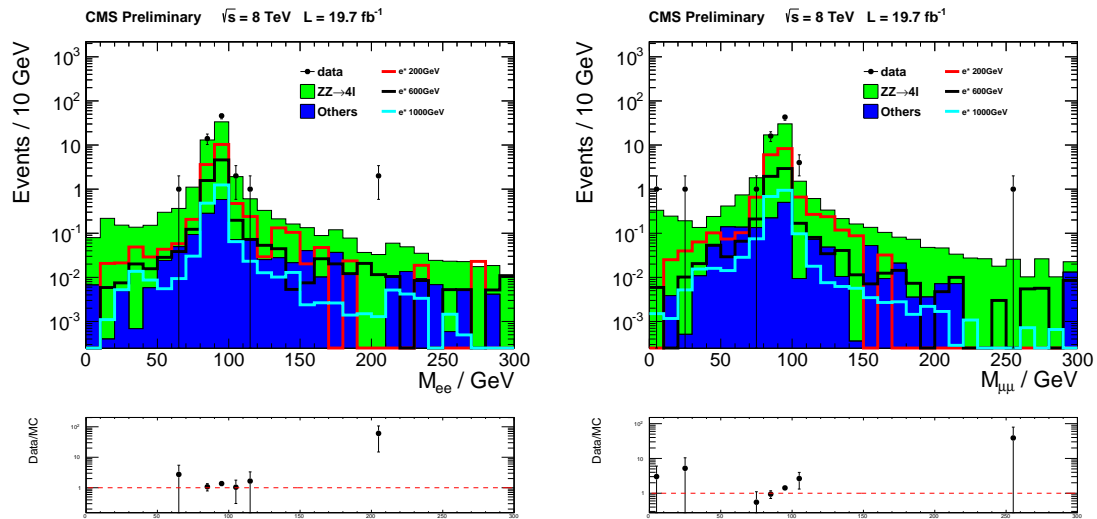


Figure 3-9: Invariant mass distribution of the selected Z before invariant mass cuts. Left: $\mu\mu^* \rightarrow 2\mu 2e$ channel, Right: $ee^* \rightarrow 2e 2\mu$ channel

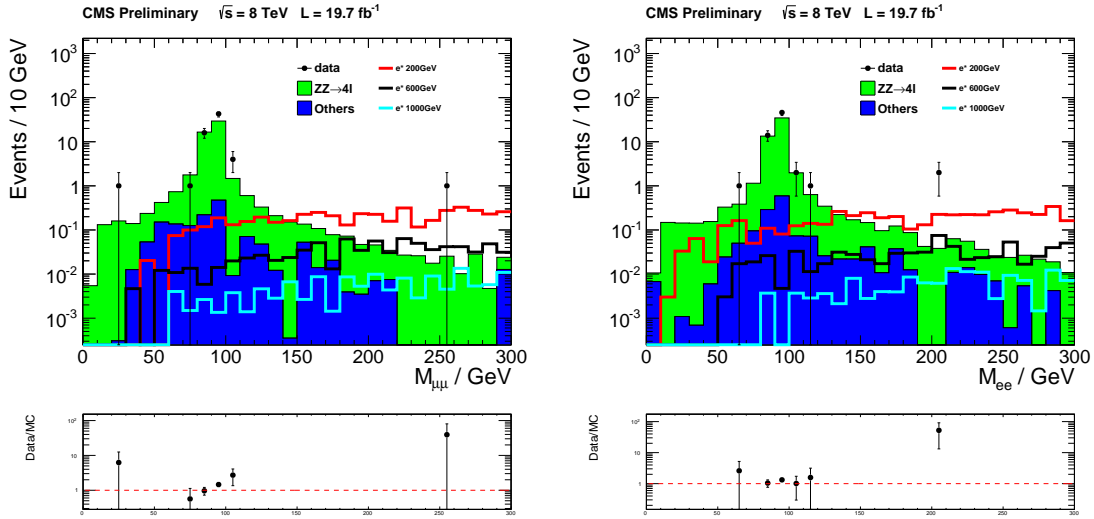


Figure 3-10: Invariant mass distribution of the vetoed Z before invariant mass cuts. Left: $\mu\mu^* \rightarrow 2\mu 2e$ channel, Right: $ee^* \rightarrow 2e 2\mu$ channel

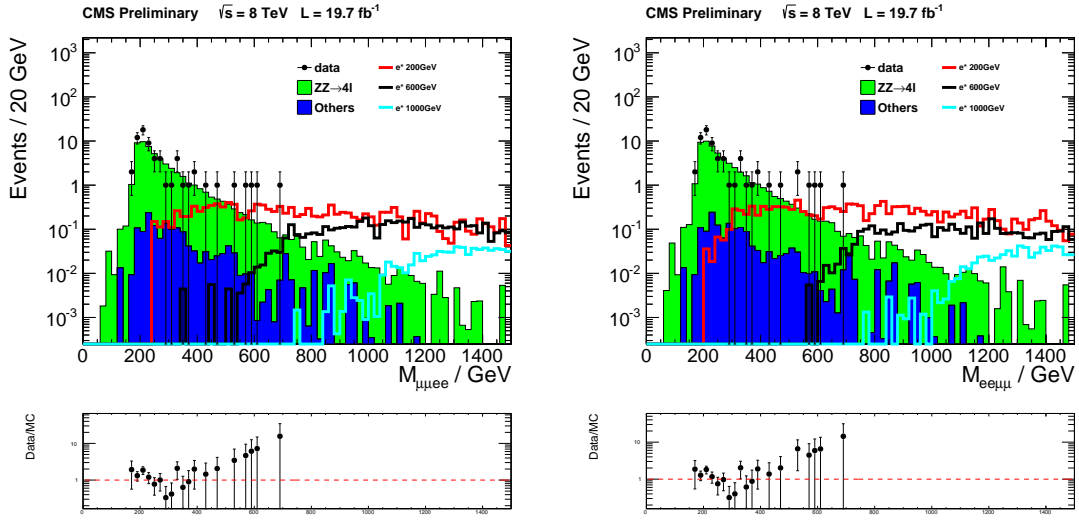


Figure 3-11: Four lepton invariant mass M_{4l} before invariant mass cuts. Left: $\mu\mu^* \rightarrow 2\mu 2e$ channel, Right: $ee^* \rightarrow 2e 2\mu$ channel

Background	$\mu\mu^* \rightarrow 4\mu$	$\mu\mu^* \rightarrow 2\mu 2e$	combined
$ZZ \rightarrow 4\mu$	33.82 ± 0.18	0.00 ± 0.00	33.82 ± 0.18
$ZZ \rightarrow 2e2\mu$	0.00 ± 0.00	50.07 ± 0.34	50.07 ± 0.34
$ZZ \rightarrow 2e2\tau$	0.00 ± 0.00	0.09 ± 0.02	0.09 ± 0.02
$ZZ \rightarrow 2\mu 2\tau$	0.13 ± 0.02	0.17 ± 0.03	0.30 ± 0.04
$WZ \rightarrow 3l\nu$	0.00 ± 0.00	0.47 ± 0.07	0.47 ± 0.07
$gg \rightarrow ZZ \rightarrow 2l'2l'$	0.01 ± 0.00	3.64 ± 0.05	3.65 ± 0.05
$gg \rightarrow ZZ \rightarrow 4l$	1.84 ± 0.02	0.01 ± 0.00	1.85 ± 0.02
ttZ	0.45 ± 0.10	0.63 ± 0.10	1.07 ± 0.14
$ttWW$	0.00 ± 0.00	0.01 ± 0.00	0.01 ± 0.00
WWZ	0.16 ± 0.03	0.26 ± 0.04	0.42 ± 0.05
WZZ	0.10 ± 0.01	0.17 ± 0.02	0.27 ± 0.02
ZZZ	0.07 ± 0.01	0.12 ± 0.01	0.19 ± 0.01
$DY Jet$	0.00 ± 0.00	0.55 ± 0.55	0.55 ± 0.55
Total	36.63 ± 0.23	56.19 ± 0.37	92.82 ± 0.42
Total (with systematics)	36.63 ± 4.86	56.19 ± 7.01	92.82 ± 8.53
Data	29	66	95
$M_{\mu^*} = 200$ GeV	2.9×10^5	2.1×10^5	5.0×10^5
$M_{\mu^*} = 1000$ GeV	1.2×10^2	9.3×10^1	2.1×10^2
$M_{\mu^*} = 1800$ GeV	1.36	1.08	2.44
$M_{\mu^*} = 2600$ GeV	0.04	0.03	0.07

Table 3.12: Event yields for $\mu\mu^* \rightarrow 4\mu$ and $\mu\mu^* \rightarrow 2\mu 2e$ without invariant mass cut. If the column includes 0.00 ± 0.00 events, the calculated number is to small for a prediction.

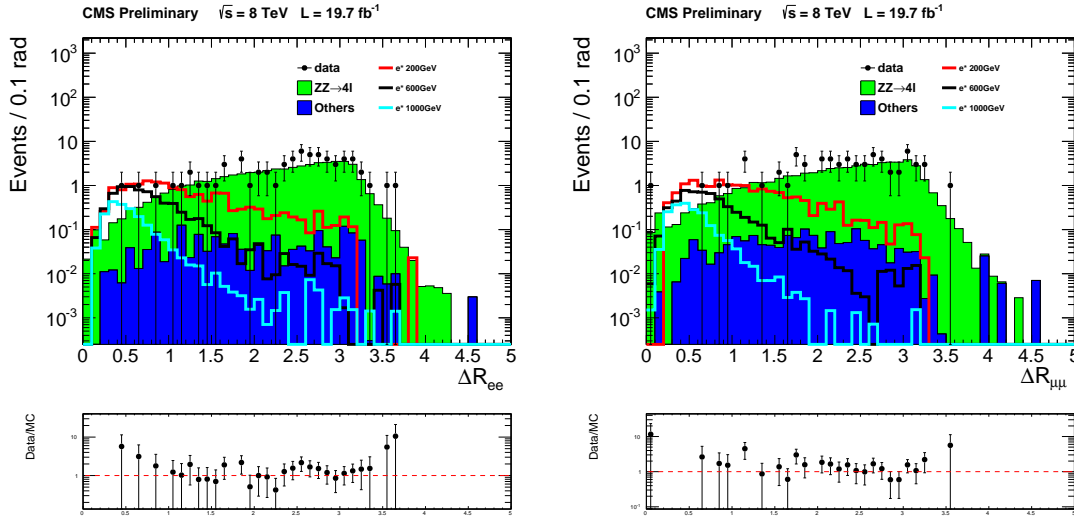


Figure 3-12: ΔR of the two muons from the Z decay before invariant mass cuts. Left: $\mu\mu^* \rightarrow 2\mu 2e$ channel, Right: $ee^* \rightarrow 2e 2\mu$ channel

Background	$ee^* \rightarrow 4e$	$ee^* \rightarrow 2e2\mu$	combined
$ZZ \rightarrow 4e$	18.65 ± 0.13	0.00 ± 0.00	18.65 ± 0.13
$ZZ \rightarrow 2e2\mu$	0.00 ± 0.00	50.97 ± 0.35	50.97 ± 0.35
$ZZ \rightarrow 2e2\tau$	0.10 ± 0.02	0.10 ± 0.02	0.20 ± 0.04
$ZZ \rightarrow 2\mu2\tau$	0.00 ± 0.00	0.18 ± 0.03	0.18 ± 0.03
$WZ \rightarrow 3l\nu$	0.03 ± 0.02	0.47 ± 0.07	0.50 ± 0.07
$gg \rightarrow ZZ \rightarrow 2l2l'$	0.01 ± 0.01	3.68 ± 0.05	3.69 ± 0.05
$gg \rightarrow ZZ \rightarrow 4l$	1.12 ± 0.01	0.01 ± 0.00	1.13 ± 0.01
ttZ	0.21 ± 0.06	0.76 ± 0.13	0.97 ± 0.14
$ttWW$	0.00 ± 0.00	0.01 ± 0.00	0.01 ± 0.00
WWZ	0.00 ± 0.00	0.25 ± 0.04	0.25 ± 0.04
WZZ	0.02 ± 0.01	0.17 ± 0.02	0.19 ± 0.02
ZZZ	0.03 ± 0.00	0.12 ± 0.01	0.15 ± 0.01
$DY Jet$	0.00 ± 0.00	0.55 ± 0.55	0.55 ± 0.55
Total	20.17 ± 0.15	57.27 ± 0.37	78.44 ± 0.40
Total (with systematics)	20.17 ± 2.84	57.27 ± 7.81	78.44 ± 8.31
Data	16	67	83
$M_{e^*} = 200$ GeV	2.1×10^5	2.2×10^5	4.3×10^5
$M_{e^*} = 1000$ GeV	7.8×10^1	8.7×10^1	1.7×10^2
$M_{e^*} = 1800$ GeV	0.86	1.08	1.94
$M_{e^*} = 2600$ GeV	0.03	0.03	0.06

Table 3.13: Events yields for $ee^* \rightarrow 4e$ and $ee^* \rightarrow 2e2\mu$ without invariant mass cut. If the column includes 0.00 ± 0.00 events, the calculated number is too small for a prediction.

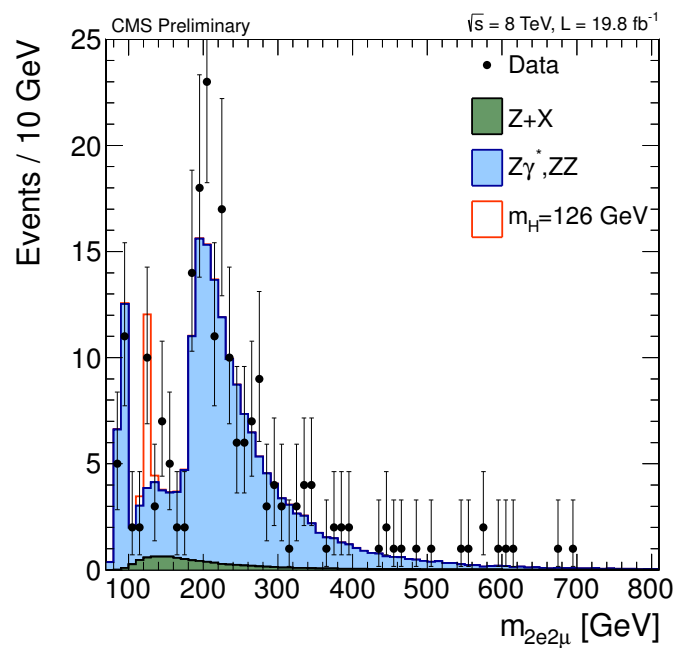


Figure 3-13: Four lepton invariant mass distribution in $H \rightarrow ZZ \rightarrow 2e2\mu$. The excess can also be observed around peak region.

After invariant mass cuts

Before applying the final selection, event yields after applying the two invariant mass cuts below is concerned.

- Mass cut on Z selection: $M_Z > 60$ GeV
- Z-Veto on non-Z pair: $M_{nonZ} > 106$ GeV

In Fig. 3-14 and Fig. 3-15 the minimum and maximum mass distribution are shown. One can also see the excited lepton mass from these plots by the shape of signal samples. Tab. 3.14 shows the event yields for the μ channels and Tab. 3.15 shows the event yields for the e^* channels. As one can see, there are only a small number of events left. The agreement between data and MC is good at this point of the analysis for all channels.

Background	$\mu\mu^* \rightarrow 4\mu$	$\mu\mu^* \rightarrow 2\mu 2e$	combined
$ZZ \rightarrow 4\mu$	3.45 ± 0.06	0.00 ± 0.00	3.45 ± 0.06
$ZZ \rightarrow 2e 2\mu$	0.00 ± 0.00	2.14 ± 0.07	2.14 ± 0.07
$ZZ \rightarrow 2\mu 2\tau$	0.02 ± 0.01	0.00 ± 0.00	0.02 ± 0.01
$WZ \rightarrow 3l\nu$	0.00 ± 0.00	0.02 ± 0.01	0.02 ± 0.01
$gg \rightarrow ZZ \rightarrow 2l 2l'$	0.00 ± 0.00	0.11 ± 0.01	0.11 ± 0.01
$gg \rightarrow ZZ \rightarrow 4l$	0.13 ± 0.01	0.00 ± 0.00	0.13 ± 0.01
ttZ	0.31 ± 0.08	0.16 ± 0.05	0.47 ± 0.09
WWZ	0.08 ± 0.02	0.09 ± 0.02	0.17 ± 0.03
WZZ	0.01 ± 0.00	0.01 ± 0.00	0.02 ± 0.00
Total	4.00 ± 0.11	2.53 ± 0.09	6.53 ± 0.14
Total (with systematics)	4.00 ± 0.52	2.53 ± 0.34	6.53 ± 0.62
Data	4	2	6
$M_{\mu^*} = 200$ GeV	2.8×10^5	2.0×10^5	4.8×10^5
$M_{\mu^*} = 1000$ GeV	1.1×10^2	9.0×10^1	2.0×10^2
$M_{\mu^*} = 1800$ GeV	1.34	1.05	2.39
$M_{\mu^*} = 2600$ GeV	0.04	0.03	0.07

Table 3.14: Events yields for $\mu\mu^* \rightarrow 4\mu$ and $\mu\mu^* \rightarrow 2\mu 2e$ after invariant mass cuts. If the column includes 0.00 ± 0.00 events, the calculated number is too small for a prediction.

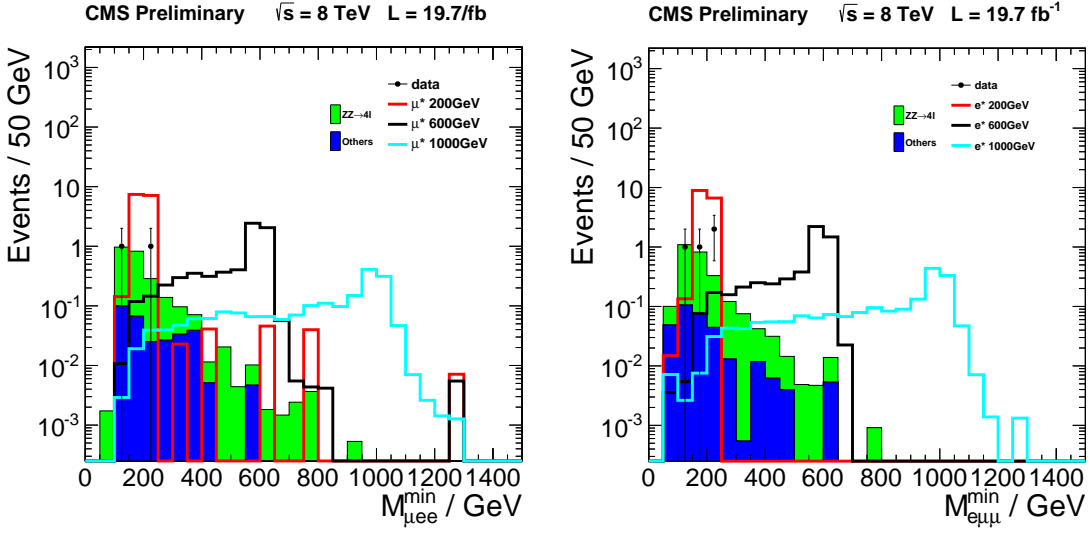


Figure 3-14: Minimum invariant mass distribution M_{min}^{3l} after invariant mass cuts.
Left: $\mu\mu^* \rightarrow 2\mu 2e$ channel, Right: $ee^* \rightarrow 2e 2\mu$ channel

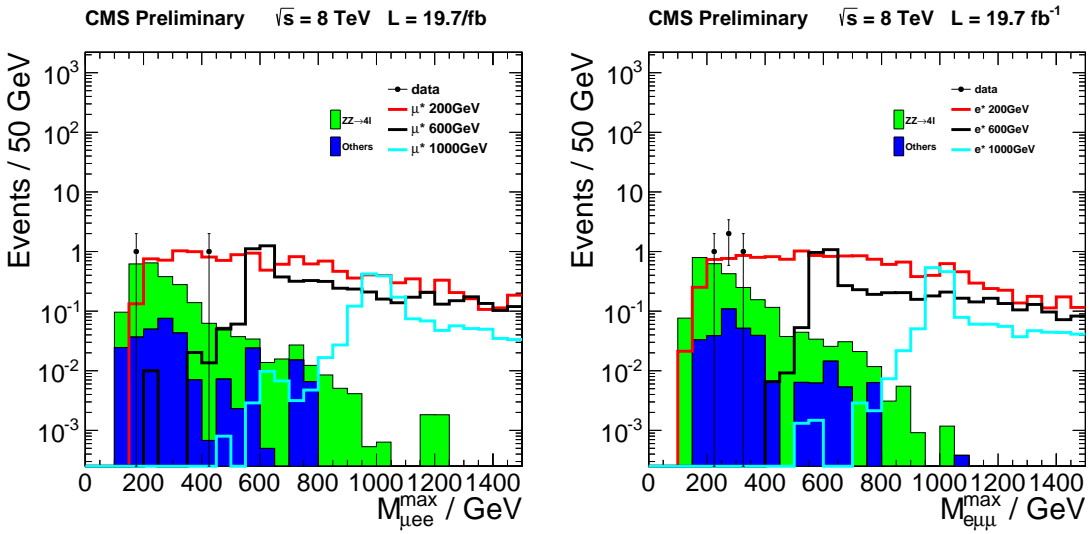


Figure 3-15: Maximum invariant mass distribution M_{max}^{3l} after invariant mass cuts.
Left: $\mu\mu^* \rightarrow 2\mu 2e$ channel, Right: $ee^* \rightarrow 2e 2\mu$ channel

Background	$ee^* \rightarrow 4e$	$ee^* \rightarrow 2e2\mu$	combined
$ZZ \rightarrow 4e$	2.66 ± 0.05	0.00 ± 0.00	2.66 ± 0.05
$ZZ \rightarrow 2e2\mu$	0.00 ± 0.00	2.32 ± 0.07	2.32 ± 0.07
$ZZ \rightarrow 2e2\tau$	0.02 ± 0.01	0.00 ± 0.00	0.02 ± 0.01
$ZZ \rightarrow 2\mu2\tau$	0.00 ± 0.00	0.02 ± 0.01	0.02 ± 0.01
$WZ \rightarrow 3l\nu$	0.03 ± 0.02	0.21 ± 0.05	0.24 ± 0.05
$gg \rightarrow ZZ \rightarrow 2l2l'$	0.00 ± 0.00	0.14 ± 0.01	0.14 ± 0.01
$gg \rightarrow ZZ \rightarrow 4l$	0.12 ± 0.00	0.00 ± 0.00	0.12 ± 0.00
ttZ	0.13 ± 0.05	0.12 ± 0.05	0.25 ± 0.08
WWZ	0.00 ± 0.00	0.10 ± 0.02	0.10 ± 0.02
WZZ	0.01 ± 0.01	0.01 ± 0.00	0.02 ± 0.01
Total	2.95 ± 0.07	2.94 ± 0.10	5.89 ± 0.12
Total (with systematics)	2.95 ± 0.41	2.94 ± 0.39	5.89 ± 0.57
Data	0	4	4
$M_{e^*} = 200$ GeV	2.0×10^5	2.1×10^5	4.1×10^5
$M_{e^*} = 1000$ GeV	7.6×10^1	8.6×10^1	1.6×10^2
$M_{e^*} = 1800$ GeV	0.84	1.06	1.90
$M_{e^*} = 2600$ GeV	0.03	0.03	0.06

Table 3.15: Events yields for $ee^* \rightarrow 4e$ and $ee^* \rightarrow 2e2\mu$ after invariant mass cuts. If the column includes 0.00 ± 0.00 events, the calculated number is too small for a prediction.

3.5 Systematic uncertainties

The following systematic uncertainties are included in this analysis:

- **Electron reconstruction:**

1. Electron energy scale: For electrons, the recommended uncertainty of 1% on the transverse electron energy E_T [36] is applied. This results in an uncertainty on the number of signal events at the 1% level. The impact on backgrounds is 0.8% in the $\mu\mu^* \rightarrow \mu\mu Z \rightarrow 2\mu 2e$ channel. In the other channel, where the electron pair does not originate from the Z-boson, the impact on background's event yield is larger due to Z-veto selection. It is 8% for $ee^* \rightarrow eeZ \rightarrow 2e 2\mu$ channel.
2. Electron energy resolution: For electron resolution, electron E_T is smeared by 1% [37]. The impact on event yield is smaller than the energy scale uncertainty and is at 0.1% level.
3. Electron ID scale factors: The systematic uncertainty on electron scale factors is 0.7%(0.6%) for electrons below 100 GeV in EB(EE) and 1.4%(0.4%) for electrons greater than 100 GeV in EB(EE) [26]. This scale factor does also include the isolation requirement.

- **Muon reconstruction:**

1. Muon momentum scale: For muons with p_T below 200 GeV, 0.2% uncertainty is applied. For muons with larger transverse momentum, a p_T depending uncertainty of 5% / TeV [30] is applied. The impact of the yield is below 0.1% for backgrounds and less than 1% for signal processes.
2. Muon resolution: To calculate the uncertainty on the resolution, a p_T smearing of 0.6% [30] is applied. The impact on the event yield is smaller than the momentum scale uncertainty.
3. Muon ID scale factors: The systematic uncertainty on muon scale factors is expected to be 0.5 % for the ID efficiency and 0.2 % for the isolation

efficiency per muon.

- **Background cross section:** For the main background $ZZ \rightarrow 4l$, an uncertainty of 15% is considered, based on SMP-12-024 [38].
- **Signal cross section:** An uncertainty of 10 % on the NLO QCD k-factor based on the PDF measurements from [1]. The k-factor has been calculated with CTEQ6 and MSTW2008. The maximum difference of 10 % is used as uncertainty.
- **Pileup simulation:** To calculate the uncertainties on the pileup simulation, we produce two pileup distributions where the minimum bias cross section is shifted by $\pm 5\%$ [39]. The impact on the event yields is less than 1%.
- **Luminosity:** The uncertainty on the luminosity is considered to be 2.6% [15].

The considered uncertainties are summarized in the Tab. 3.16-3.17. These systematics are included in the limit computation. Since this analysis use a single bin counting experiment, the error on the event yield by resolution and scale uncertainties is very small, also if the effect on bin in the histogram is large.

Systematic	$m_{\mu^*} = 200$ GeV	$m_{\mu^*} = 2600$ GeV	Backgrounds
Trigger efficiency	negligible	negligible	negligible
Muon ID efficiency	1%	1%	1%
Muon Iso efficiency	0.4%	0.4%	0.4%
Muon momentum scale	0.3%	0.4%	1.1%
Muon momentum resolution	0.2%	< 0.1%	0.2%
Electron ID efficiency	2.0%	2.8%	1.5%
Electron energy scale	0.4%	0.2%	0.8%
Electron energy resolution	0.2%	< 0.1%	0.1%
ZZ background	-	-	15%
Signal cross section	10%	10%	-
pileup simulation	0.6%	0.1%	0.2%
Luminosity	2.6%	2.6%	2.6%

Table 3.16: Summary of systematic uncertainties on signal and background yields for the $\mu\mu^* \rightarrow 2\mu 2e$ channel. Here, the two electrons come from the boosted Z and the Z Veto is applied to the muon pair. The uncertainties are the combined ones for all leptons, the considered single lepton uncertainties are summarized in the text.

Systematic	$m_{e^*} = 200$ GeV	$m_{e^*} = 2600$ GeV	Backgrounds
Trigger efficiency	negligible	negligible	negligible
Muon ID efficiency	1%	1%	1%
Muon Iso efficiency	0.4%	0.4%	0.4%
Muon momentum scale	0.3%	0.8%	0.2%
Muon momentum resolution	0.1%	< 0.1%	0.1%
Electron ID efficiency	2.2%	3.3%	1.6%
Electron energy scale	0.2%	< 0.1%	8%
Electron energy resolution	0.1%	< 0.1%	0.1%
ZZ background	-	-	15%
Signal cross section	10%	10%	-
pileup simulation	0.2%	0.5%	0.4%
Luminosity	2.6%	2.6%	2.6%

Table 3.17: Summary of systematic uncertainties on signal and background yields for the $ee^* \rightarrow 2e 2\mu$ channel. Here, the two muons come from the boosted Z and the Z Veto is applied to the electron pair. The uncertainties are the combined ones for all leptons, the considered single lepton uncertainties are summarized in the text.

Chapter 4

Results and conclusion

In this chapter, the final selection is finally applied. The signal, background, and data count after this selection is then be used to perform the estimation of upper limits of excited leptons. This chapter also make comparisons to $\mu\mu^* \rightarrow 4\mu$ and $ee^* \rightarrow 4e$ channels. In the end, the final excited muon limit is shown by combining the results of $\mu\mu^* \rightarrow 2\mu 2e$ and $\mu\mu^* \rightarrow 4\mu$ channels, and the same is done for limit of excited electron.

4.1 Cross section limit computation

As no significant excess can be observed, there is no evidence for existence of excited leptons. Thus, the sight now turns to set the limit for the excludable signal cross section as well as the region in the space of the excited lepton mass to the compositeness scale parameter Λ . The calculation of the 95% CL excluded cross section is done with a Bayesian approach by using the statistical tool provided by the CMS collaboration that is based on ROOSTATS [40, 41].

The statistical analysis of each channel is performed as a single bin counting experiment that is performed for each signal point individually. The two channels of e^* and μ^* respectively are afterward combined to a single limit in order to further expand the excluded region.

4.2 Optimization of the final selection

For our final selection, we look at the minimum-maximum three-body invariant mass plane. The signal has the shape of an inverted L in this plane. By adding a minimum invariant mass cut (vertical, left area) and a maximum invariant mass cut (horizontal, above area), the background can be discriminated easily. Fig. 4-1 shows the minimum-maximum invariant mass plane for both $\mu\mu^* \rightarrow 2\mu 2e$ and $ee^* \rightarrow 2e 2\mu$ channels with different invariant masses.

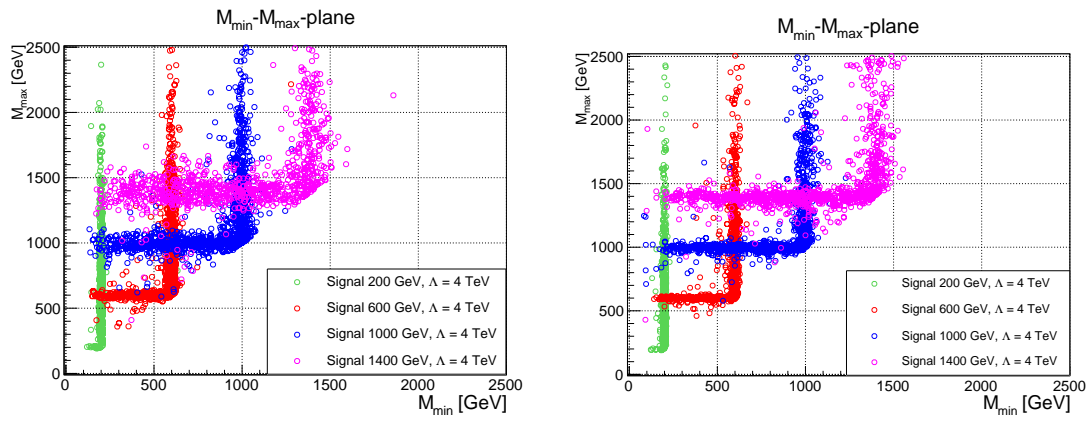


Figure 4-1: 2-dimensional minimum-maximum invariant mass distribution after invariant mass cuts for different l^* masses. Left: $\mu\mu^* \rightarrow 2\mu 2e$ channel. Right: $ee^* \rightarrow 2e 2\mu$ channel.

The boundaries of the final selection depend on the mass of the excited leptons. Fig. 4-3 shows the selection of the boundaries for an invariant mass of 600 GeV. There are four cuts set: A lower cut von M_{min} , a higher cut on M_{min} , a lower cut on M_{max} and a higher cut on M_{max} . The most important cuts of this four are the higher M_{min} and the lower M_{max} cuts, which do most effort on separating signal and background. For the definition of the cut ranges, the best expected limit for the lower maximum invariant mass cut was calculated. Now, a range from optimized lower M_{max} cut to the central mass of each l^* samples is obtained. Then, we apply this range to upper M_{max} cut, upper M_{min} cut, and lower M_{min} cut to form a symmetric signal region for each signal sample. Tab. 4.1 - 4.2 show the range and the event yields for the different l^* masses and Fig. 4-2 shows the acceptance \times efficiency after lepton selection, after

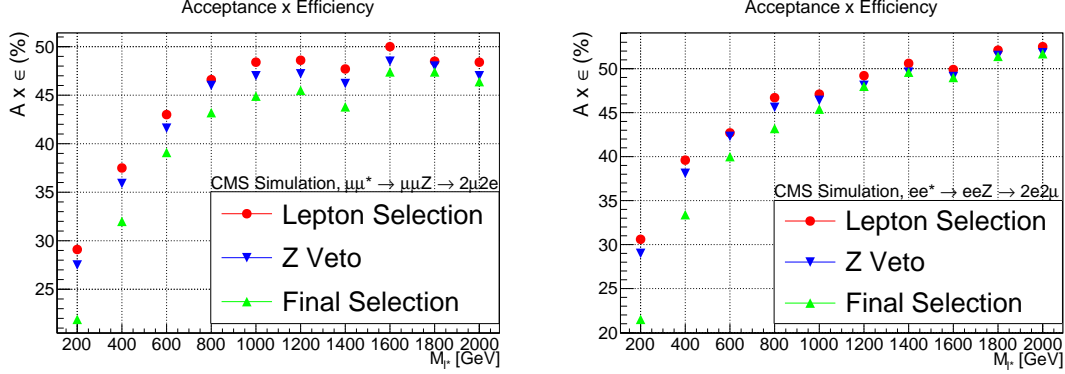


Figure 4-2: Acceptance \times Efficiency for different cut stages: Lepton selection, Z veto and final selection.

the Z-veto selection and after the final selection.

$m(\mu^*)$ [GeV]	$M_{min} - M_{max}$ Cut [GeV]	Data	BG (# Events)	ϵ_{all}
200	196-204	0	0.23 ± 0.05	22.3%
400	376-424	1	0.14 ± 0.03	32.8%
600	540-660	0	0.07 ± 0.03	39.8%
800	720-880	0	0.04 ± 0.01	44.3%
1000	850-1150	0	0.01 ± 0.01	46.1%
1200	1000-1400	0	0.00 ± 0.00	46.7%
1400	1200-1800	0	0.01 ± 0.01	45.0%
1600	1200-2200	0	0.01 ± 0.01	48.4%
1800	1200-2600	0	0.01 ± 0.01	48.7%
2000	1200-3000	0	0.01 ± 0.01	47.6%
2200	1200-3400	0	0.01 ± 0.01	47.4%
2400	1200-3800	0	0.01 ± 0.01	48.2%
2600	1200-4200	0	0.01 ± 0.01	45.5%

Table 4.1: Cut ranges for the L shape cuts, corresponding event yields and signal efficiencies $\mu\mu^* \rightarrow 2\mu 2e$.

Looking at the Tab. 4.1-4.2, it can be seen that the selected signal regions do not cover the complete parameter space. Especially in the low mass regions, there are gaps between the search regions that might lead to a case where a potential excited lepton could not be discovered. Those gaps are closed by additional L-shaped search regions that are determined as follows. The 4e-channel is chosen to estimate the new regions as it has the best mass resolution and thus the most narrow windows.

$m(e^*)$ [GeV]	$M_{min} - M_{max}$ Cut [GeV]	Data	BG (# Events)	ϵ_{all}
200	196-204	0	0.24 ± 0.05	22.4%
400	384-416	0	0.09 ± 0.02	34.6%
600	552-648	0	0.08 ± 0.02	41.6%
800	728-872	0	0.02 ± 0.01	44.7%
1000	860-1140	0	0.02 ± 0.01	47.3%
1200	860-1540	0	0.02 ± 0.01	49.7%
1400	860-1940	0	0.02 ± 0.01	51.1%
1600	860-2340	0	0.02 ± 0.01	51.1%
1800	860-2740	0	0.02 ± 0.01	53.7%
2000	860-3140	0	0.02 ± 0.01	53.8%
2200	860-3540	0	0.02 ± 0.01	52.3%
2400	860-3940	0	0.02 ± 0.01	52.8%
2600	860-4340	0	0.02 ± 0.01	52.6%

Table 4.2: Cut ranges for the L shape cuts, corresponding event yields and signal efficiencies $ee^* \rightarrow 2e2\mu$.

For the windows given by the signal MC, the width was plotted depending on the e^* -Mass. The width and the position of the new windows is estimated by linear interpolation. The positions are used in all channels, while the correponding width has to be estimated for each channel individually.

Measured data, as well as the background expectation in this new search regions can be drived from the distribution. As there is no corresponding MC, this information is not available for the signal. Estimate the signal contribution by a fit on the points we have from the signal MC.

The channels containing muons have a much higher $A \times \epsilon$ because of the higher efficiency of the high- p_T muon ID. As the numbers show, the lose of efficiency due to the L shape cut is very small while we can discriminate the background to a small amount of events. This characteristic returns a very good signal over brackground ratio.

4.3 Limit computation

The selection defined in section 4.2 and the limit setting tool are used to calculate observed and expected limits for all four channels. The inputs from Tab. 4.1 - 4.2 are used for the limit calculation. The calculated cross section limits depend on the compositeness scale Λ (here, $f = f' = 1$ is assumed). One natural point for limit setting is the point where the l^* -mass and the compositeness scale have the same value.

4.3.1 Limits for excited muons μ^*

Fig. 4-4 and 4-5 show the cross section limits and the limits on the compositeness scale for $\mu\mu^* \rightarrow 4\mu$ and $\mu\mu^* \rightarrow 2\mu 2e$ depending on the μ^* -mass. The black lines show the signal cross section for different values of Λ . From those plots, the channel $\mu\mu^* \rightarrow 4\mu$ excited muons can be excluded up to a mass of 1.65 TeV for $\Lambda = M_{\mu^*}$. In the channel $\mu\mu^* \rightarrow 2\mu 2e$, the limit is set to 1.60 TeV.

4.3.2 Limits for excited leptons e^*

For excited electrons, the same limits as for the excited muons search has been calculated. Fig. 4-6 and 4-7 show the cross section limits and the limits on the compositeness scale for $e^* \rightarrow 4e$ and $ee^* \rightarrow 2e 2\mu$. Here, both channels exclude masses up to 1.60 TeV for $\Lambda = M_{e^*}$.

Depending on the limits of both channels, a combination has been done. This combination leads to an exclusion limit of 1.75 TeV for excited muons from Fig. 4-8. The limit on excited electrons can be set to 1.7 TeV for $\Lambda = M_{e^*}$ as shown in 4-9. In all cases, the expected and observed limits are close to each other.

The limit plots show some striking features. Looking at Fig. 4-4 to 4-9 it can be seen that on the one hand, the error bands are mostly asymmetric around the median expected limit. On the other hand, the 1σ - and sometimes also the 2σ -band drop to a value very close to the dashed line of the median expected limit. Both effects have the same reason which is the low background expectation of below one event in

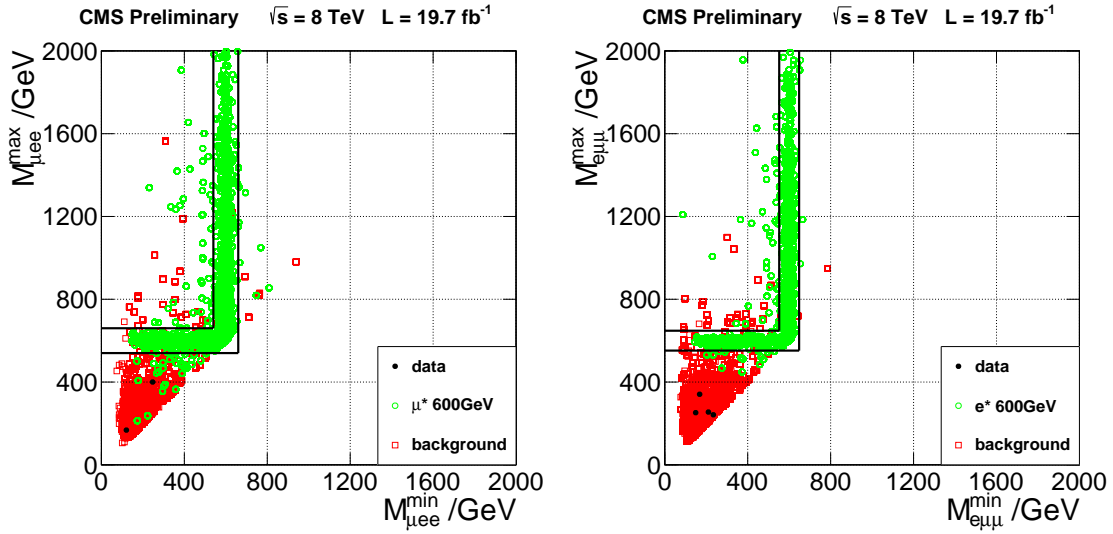


Figure 4-3: 2-dimensional minimum-maximum invariant mass distribution after invariant mass cuts. Left: $\mu\mu^* \rightarrow 2\mu 2e$ channel. Right: $ee^* \rightarrow 2e 2\mu$ channel.

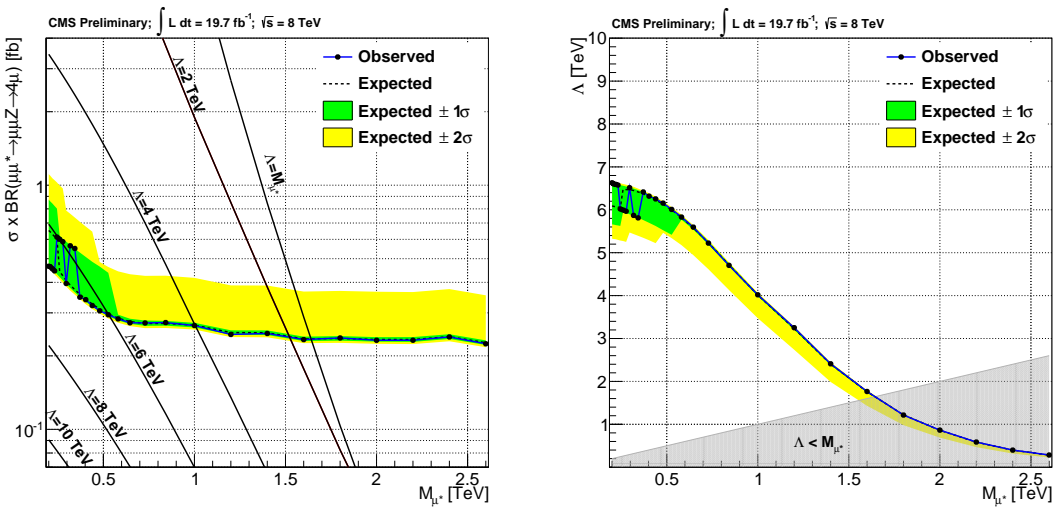


Figure 4-4: Cross section and Λ limit for $\mu\mu^* \rightarrow 4\mu$.

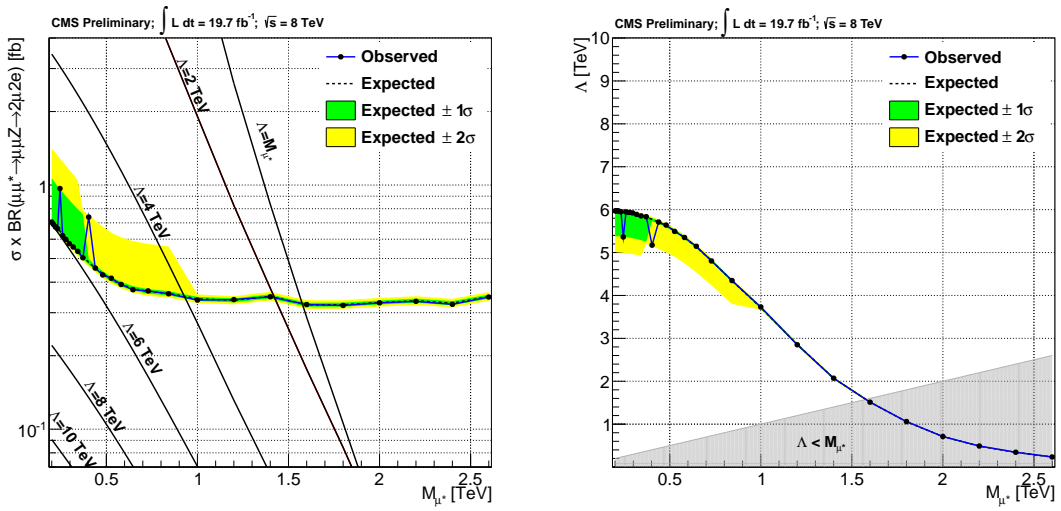


Figure 4-5: Cross section and Λ limit for $\mu\mu^* \rightarrow 2\mu 2e$.

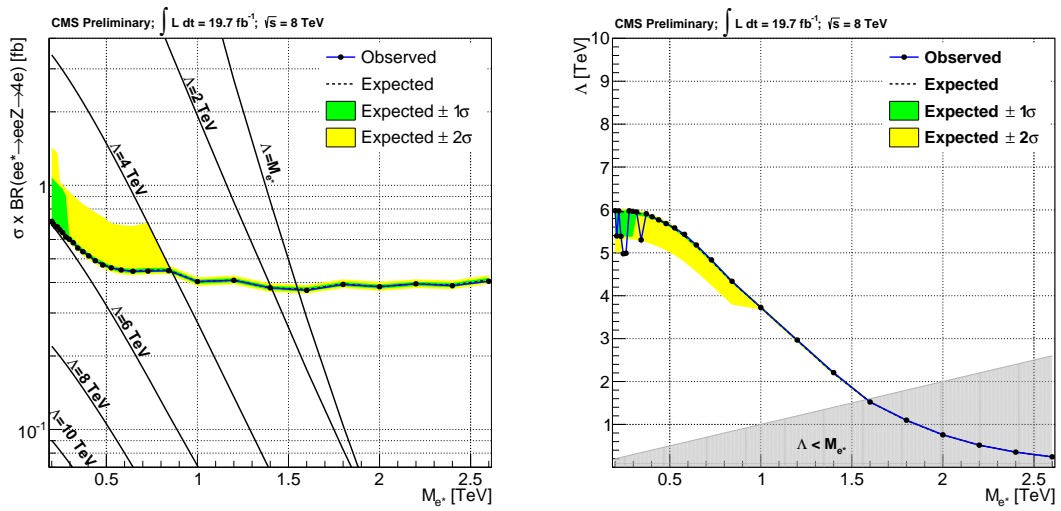


Figure 4-6: Cross section and Λ limit for $ee^* \rightarrow 4e$.

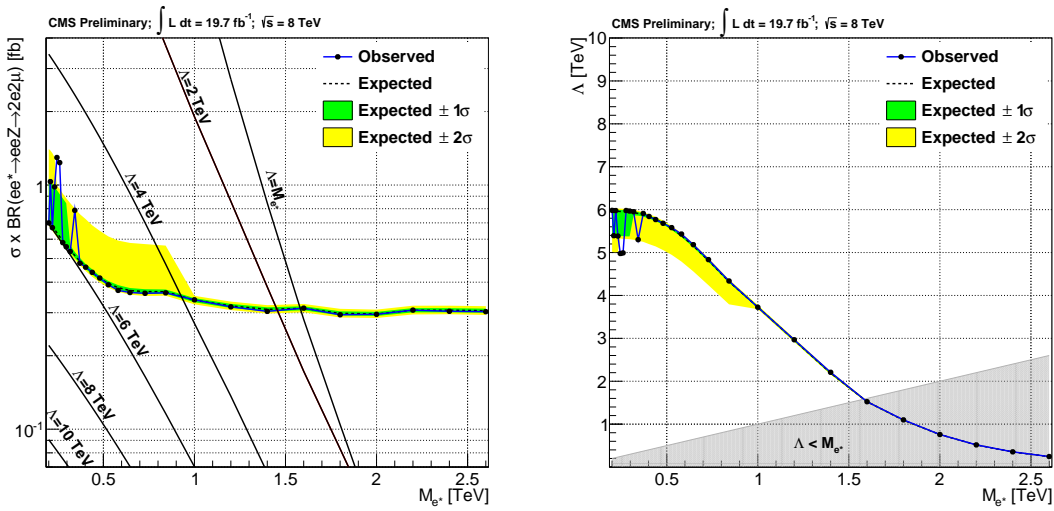


Figure 4-7: Cross section and Λ limit for $ee^* \rightarrow 2e2\mu$.

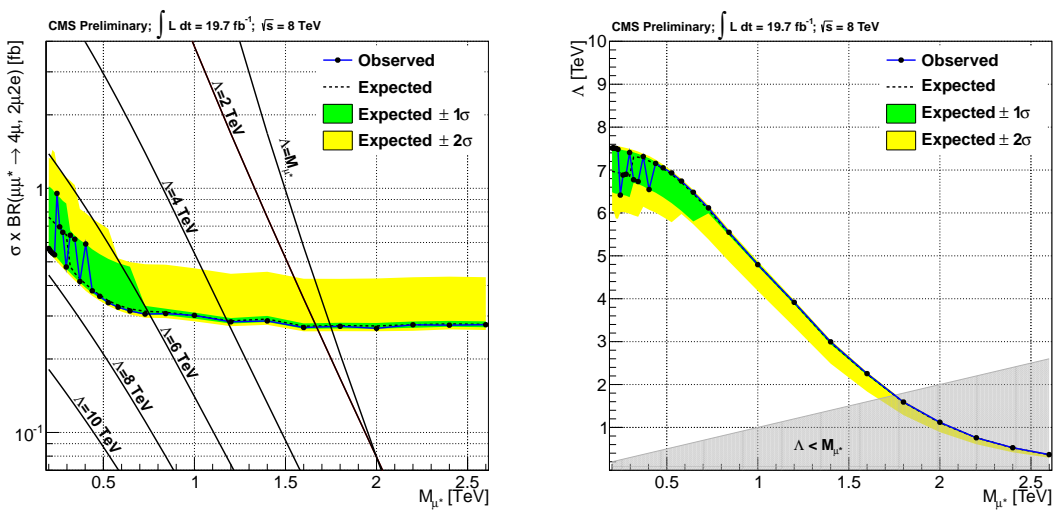


Figure 4-8: Combined cross section and Λ limit for $\mu\mu^* \rightarrow 4l$.

the search regions (comp. Tab. 4.1 - 4.2). During the limit computation, repeatedly toy-experiments are diced. When the background expectation is low, those are manly varied in the upper direction as it is not possible to reach under zero. Thus the asymmetric error bands can be explained. When the background expectation becomes even lower as in the high mass search regions, the limit calculation is not able to iterate higher intger event assumptions and one after another, first the 1σ - and later on also the 2σ -quantile drop into the 0-event assumption resulting in the very narrow error bands.

4.4 Conclusion

For the first time, a search for excited electrons and muons is performed in the channels with four leptons in the final states using pp collision data at $\sqrt{s} = 8TeV$. No evidence of new physics is observed. Combining the respective two search channels, excited electrons with $M_e < 1.70TeV$ and excited muons with $M_\mu < 1.75TeV$ are excluded for the compositeness scale equals to the excited lepton mass ($M_{l^*} = \Lambda$).

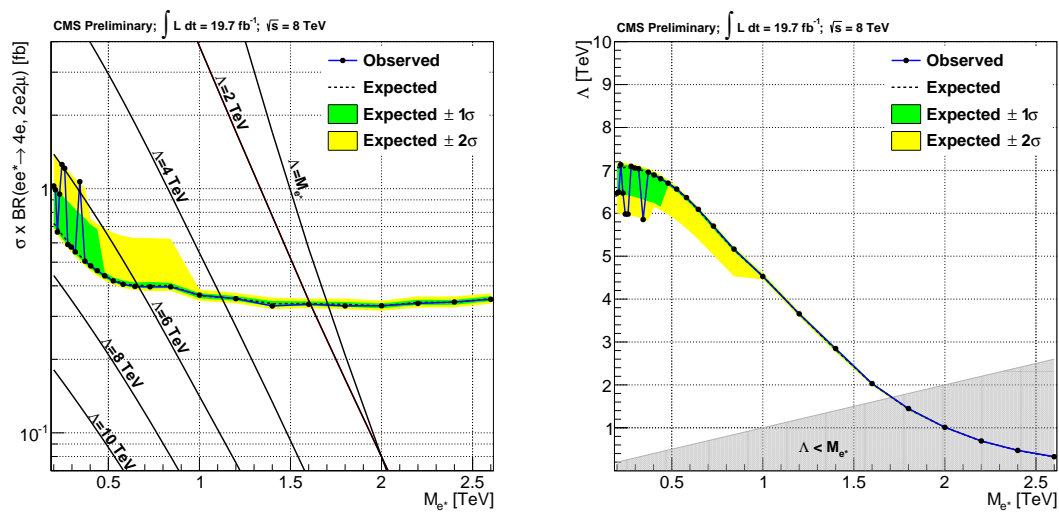


Figure 4-9: Combined cross section and Λ limit for $ee^* \rightarrow 4l$.

Bibliography

- [1] Swapan Majhi. QCD corrections to excited lepton (pair)production at LHC. 2012.
- [2] J. Pati and A. Salam. Lepton number as the fourth color. *Phys. Rev. D*, 10:275, 1974.
- [3] U. Baur, M. Spira, and P.M. Zerwas. Excited-quark and -lepton production at hadron colliders. *Phys. Rev. D*, 42:815, 1990.
- [4] E.J. Eichten, K.D. Lane, and M.E. Peskin. New tests for quark and lepton substructure. *Phys. Rev. Lett.*, 50:811, 1983.
- [5] CDF Collaboration. Search for excited and exotic electrons in the $e\gamma$ decay channel in $p\bar{p}$ collisions at $\sqrt{s}=1.96$ tev. *Phys. Rev. Lett.*, 94:101802, 2005.
- [6] CDF Collaboration. Search for excited and exotic electrons in the $\mu\gamma$ decay channel in $p\bar{p}$ collisions at $\sqrt{s}=1.96$ tev. *Phys. Rev. Lett.*, 97:191802, 2006.
- [7] D0 Collaboration. Search for excited muons in $p\bar{p}$ collisions at $\sqrt{s}=1.96$ tev. *Phys. Rev.*, D73:111102, 2006.
- [8] D0 Collaboration. Search for excited electrons in $p\bar{p}$ collisions at $\sqrt{s}=1.96$ tev. *Phys. Rev.*, D77:091102, 2008.
- [9] Exotica Resonances Group. Physicsresults exo10016. <https://twiki.cern.ch/twiki/bin/view/CMSPublic/PhysicsResultsEXO10016>.
- [10] Sunanda Banerjee, Satyaki Bhattacharya, and Shilpi Jain. Search for excited electron in pp collisions at $\sqrt{s}=7$ tev in the cms experiment with $4.7 fb^{-1}$ of data. *CMS Analysis Note: AN-11-452*, 2012.
- [11] J. Caudron, K. Hoepfner, I. Svintradze1, Y. Maravin, C.-M. Kuo, and S. Bahinipati. Search for excited muons in proton-proton collisions at $\sqrt{s}=7$ tev with the cms detector. *CMS Analysis Note: AN-12-013*, 2012.
- [12] ATLAS Collaboration. Search for excited leptons in proton-proton collisions at $\sqrt{s} = 7$ TeV with the ATLAS detector. 2012.
- [13] Torbjorn Sjostrand, Stephen Mrenna, and Peter Z. Skands. PYTHIA 6.4 Physics and Manual. *JHEP*, 05:026, 2006.

- [14] K. Hagiwara and K. Hikasa. Searches for quark and lepton compositeness. *The European Physical Journal C - Particles and Fields*, 15(1-4):852–860, 2000.
- [15] CMS Collaboration. ”cms luminosity based on pixel cluster counting - summer 2013 update”. *”CMS PAS LUM-13-001”*, 2013.
- [16] John Allison et al. Geant4 developments and applications. *IEEE Trans. Nucl. Sci.*, 53:270, 2006.
- [17] Johan Alwall et al. MadGraph/MadEvent v4: the new web generation. *JHEP*, 09:028, 2007.
- [18] Simone Alioli, Paolo Nason, Carlo Oleari, and Emanuele Re. NLO vector-boson production matched with shower in POWHEG. *JHEP*, 07:060, 2008.
- [19] CMS Collaboration. Physics TDR volume I, The CMS Physics Technical Design R I. *CERN-LHCC-2006-001*, page 521pp, 2006.
- [20] W Adam, R Frhwirth, A Strandlie, and T Todorov. Reconstruction of electrons with the gaussian-sum filter in the cms tracker at the lhc. *Journal of Physics G: Nuclear and Particle Physics*, 31(9):N9, 2005.
- [21] Wolfgang Adam, Boris Mangano, Thomas Speer, and Teddy Todorov. Track Reconstruction in the CMS tracker. Technical Report CMS-NOTE-2006-041, CERN, Geneva, Dec 2006.
- [22] H. Bethe and W. Heitler. On the stopping of fast particles and on the creation of positive electrons. *Proceedings of the Royal Society of London. Series A*, 146(856):83–112, 1934.
- [23] <https://twiki.cern.ch/twiki/bin/viewauth/CMS/EgCommissioningAndPhysicsDeliverables>.
- [24] <https://twiki.cern.ch/twiki/bin/view/CMS/HEEPElectronID>.
- [25] <https://twiki.cern.ch/twiki/bin/viewauth/CMS/BoostedZToEEModIso>.
- [26] <https://twiki.cern.ch/twiki/bin/viewauth/CMS/HEEPEfficiencies>.
- [27] Performance of muon identification in pp collisions at $s^{**0.5} = 7 \text{ TeV}$. Technical Report CMS-PAS-MUO-10-002, CERN, 2010. Geneva, 2010.
- [28] Exotica Muon Group. High pt muons. <https://twiki.cern.ch/twiki/bin/viewauth/CMS/ExoticaExcitedMuon>.
- [29] <https://twiki.cern.ch/twiki/bin/view/CMS/MuonReferenceEffs>.
- [30] <https://twiki.cern.ch/twiki/bin/view/CMS/MuonReferenceResolution>.
- [31] <https://twiki.cern.ch/twiki/bin/view/CMSPublic/SWGuideMuonId>.
- [32] <https://twiki.cern.ch/twiki/bin/view/CMS/MuonTagAndProbe>.

- [33] The CMS Collaboration. Search for narrow spin-2 resonance decaying to Z bosons in the semileptonic final state. <http://cds.cern.ch/record/1596494>, 2013.
- [34] <https://twiki.cern.ch/twiki/bin/view/CMS/PileupMCReweightingUtilities>.
- [35] I. Puljak E. Di Marco. Measurement of the production and decay of a higgs boson in the four-lepton final state. *CMS Analysis Note: AN-13-108*, 2013.
- [36] CMS Collaboration. Ecal detector performance, 2011 data. *CMS Performance Note: DP-12-007*, 2012.
- [37] Zprime group. Search for heavy resonances in dileptons. *CMS Analysis Note: AN-12-415*, 2012.
- [38] The CMS Collaboration. Measurement of the w^+w^- and zz production cross section in pp collisions at $\sqrt{s} = 8$ tev. 2013.
- [39] <https://twiki.cern.ch/twiki/bin/view/CMS/PileupSystematicErrors>.
- [40] G. K. et. al. Roostatscl95: cross section in a counting experiment. <https://twiki.cern.ch/twiki/bin/viewauth/CMS/RooStatsCl95>.
- [41] Higgs Statistic Group. Documentation of the roostats-based statistics tools for higgs pag. <https://twiki.cern.ch/twiki/bin/viewauth/CMS/SWGuideHiggsAnalysisCombinedLimit>.